Divergent role of CD8 T cells with distinct metabolic phenotypes during curative radio-immunotherapy in hot versus cold tumors

Alexa R. Heaton,[1,2,3]* Nathaniel J. Burkard,[3] Anqi Gao,[4] Anna Hoefges,[2] Arika S. Feils,[2] Samantha K. Burkard,[6] Mildred A. Felder,[2] Noah W. Tsarovsky,[2] Dan V. Spiegelman,[2] Garrett M. Lublin,[5] Alina A. Hampton,[2] Aurora D'Amato,[7] Huy Q. Dinh,[4,8] Alexander L. Rakhmilevich,[2] Amy K. Erbe,[2] Paul M. Sondel,[9] Melissa C. Skala[1,3,10]**

[1]Morgridge Institute for Research, Madison, WI, USA
[2]Department of Human Oncology, University of Wisconsin, Madison, WI, USA
[3]Department of Biomedical Engineering, University of Wisconsin, Madison, WI, US
[4]McArdle Laboratory for Cancer Research, University of Wisconsin, Madison, WI, USA
[5]Department of Neuroscience, University of Wisconsin, Madison, WI, USA
[6]Department of Computer Sciences, University of Wisconsin, Madison, WI, USA
[7]Global Health Institute, University of Wisconsin, Madison, WI, USA
[8]Department of Biostatistics and Medical Informatics, University of Wisconsin, Madison, WI, USA
[9]Department of Pediatrics and Department of Human Oncology, University of Wisconsin, Madison, WI, USA
[10]Lead contact
*Correspondence: aheaton@morgridge.org
**Correspondence: mcskala@wisc.edu

SUMMARY

Immunotherapy has potential for impactful cancer cures by empowering patients' own immune cells. We developed a radio-immunotherapy regimen that can cure large immunologically hot and cold murine tumors. Here we explored the divergent role of CD8 T cells during this radio-immunotherapy in contrasting hot colon carcinoma versus cold melanoma models. We introduced an immunocompetent mouse model with mCherry expressing CD8 T cells to provide immune cell tracking *in vivo*. We investigated single-cell function, metabolism, and gene expression changes with temporal context using flow cytometry, *in vivo* multiphoton imaging, single-cell RNA sequencing, and multiplexed immunofluorescence to determine the underlying mechanisms. We found that in contrast to the hot colon carcinoma model, CD8 T cells from the cold melanoma model do not drive tumor cures, despite getting activated, possibly due to a static oxidative metabolism and exhausted phenotype as well as down regulation of tumor MHC-I expression. These findings have implications for improving immunotherapy response in immunologically cold cancers.

KEYWORDS

CD8 T cells, melanoma, colon carcinoma, single cell, tumor immunology, radiation therapy, immunotherapy, metabolism, fluorescence lifetime imaging microscopy, single cell RNA sequencing

INTRODUCTION

Immunotherapy has gained traction in the last 15 years as a class of therapies with long-term benefit for many patients.[1] Despite this progress, the majority of cancer patients are not yet benefiting from immunotherapy.[2,3] To overcome this lack of response, our lab and others have focused on combining immunotherapies with synergistic immunomodulatory radiation therapy that can produce durable tumor responses across many solid tumors.[3–12] This work mirrors what is seen in the clinic where implementation of immune checkpoint inhibitors (ICI) over the last 15 years has improved cures, though long-term survival is mostly achieved when combination therapy is given.[3,13–15] Our recent preclinical work has focused on developing therapeutic solutions to treat an immunologically cold model of melanoma where immune infiltration is limited, major histocompatibility complex class I (MHC-I) expression is very low, and there is

no response to ICI – though the radio-immunotherapy regimen is effective.[9,11,16–19] Here, we deeply characterize the immune response and determine underlying mechanisms that drive this curative radio-immunotherapy combination.

Within the immuno-oncology field, over 80% of immunotherapy products in clinical trials work via CD8 T cells,[1,20] the cytotoxic cells of the adaptive immune system.[21–23] In the context of cancer, numerous barriers can prevent anti-tumor CD8 T cell function. Physical barriers include dense extracellular matrix and abnormal vasculature that exclude tumor infiltration by immune cells.[24–27] Suppressive cell types including tumor cells, fibroblasts, myeloid derived suppressor cells, and others can also dampen or even terminate CD8 T cell function via cell signaling, upregulation of checkpoint molecules, downregulation of MHC-I, and secretion of toxic molecules within the tumor microenvironment (TME).[27–40] Metabolic barriers are also prevalent, as CD8 T cells must compete for oxygen and nutrients with dysregulated tumor cells within a toxic TME.[41–50] Metabolic shifts often precede functional shifts and have been correlated to immune cell role and phenotype – providing a window into CD8 T cell function.[45,50–58] Methods that can quantify these metabolic shifts in living animals may provide a deeper understanding of tumor and immune cell metabolism during tumorigenesis and treatment, which is important for developing more effective immunotherapy. Additionally, there is a need for methods that can quantify these metabolic shifts in a noninvasive way to avoid disturbing native biology in living animals. Optical metabolic imaging (OMI) of endogenous metabolic co-enzymes can address this issue by providing label-free metabolic readouts in live, *in vivo* samples.

We have addressed these issues by establishing label-free OMI techniques to probe single-cell function, phenotype, and therapeutic response within tumors in living animals. Specifically, this imaging relies on autofluorescence from NAD(P)H and FAD, which are electron shuttles that drive most metabolic processes in the cell.[59,60] We can image and quantify intensity-based changes – related to the concentration of each molecule within the cell – and lifetime-based changes – defined as the time it takes for a molecule to relax back to the ground state after photon excitation, which informs on protein binding activity and molecular microenvironment. Protein-bound FAD and free NAD(P)H have a shorter lifetime (τ_1) while free FAD and protein-bound NAD(P)H have a longer lifetime (τ_2). The fractional contribution of coenzyme in each conformation is denoted by α_1 and α_2.[61–64] We have used this technology to gain insights into cancer and immune cell metabolism including metabolic differences between healthy and cancerous tissues[65,66] as well as immune cell metabolic shifts during activation[67–70] and immunotherapy.[71] We expand here on this previous work by performing *in vivo* tumor metabolic imaging during a curative radio-immunotherapy regimen.

Here, we investigated the therapeutic mechanisms of a curative radio-immunotherapy combination on two contrasting tumor models: immunologically hot MC38 colon carcinoma and immunologically cold B78 melanoma. We determined which immune cell populations drive tumor response and temporal changes within the TME during treatment, with a focus on CD8 T cells. We reported and used an immunocompetent mouse model with CD8 T cells that express mCherry to easily track and monitor CD8 T cell dynamics *in vivo*. We quantified immune and tumor cell metabolic changes using single-cell label-free OMI in live mouse tumors and correlate these findings with functional changes. Additionally, we examined single-cell gene expression changes to better clarify the divergent mechanisms underlying these hot versus cold tumor models. Overall, we employed a multimodal single-cell approach to investigate the divergent roles of CD8 T cells during radio-immunotherapy cures, in hot versus cold tumors, to probe the underlying mechanisms related to immunotherapy response.

RESULTS

CD8-mCherry reporter mouse model shows high specificity of mCherry expression to CD8 T cells

To facilitate *in vivo* imaging of dynamic CD8 T cells, we created a CD8-mCherry reporter mouse model where CD8 cells express the red fluorescent protein mCherry (**Fig. S1A**). To characterize these mice, CD3+ splenic T cells were isolated from both C57BL/6J wild type and CD8-mCherry reporter mice and the T cells

were imaged *in vitro* via OMI. All T cells contained NAD(P)H while only the reporter mouse expressed mCherry in ~50% of the splenic T cells, the CD8 subset (**Fig. S1B**). Additionally, multiplexed immunofluorescence (mIF) images of untreated B78 melanoma tumors and spleens from reporter mice showed that mCherry signal is only expressed on cells that also co-express CD8. There is no free mCherry signal nor mCherry signal colocalizing with CD4 (**Fig. S1C**), suggesting that the knock-in near the CD8α allele was specific with no off-target expression. Flow cytometry of untreated B78 melanoma tumors and spleens from CD8-mCherry reporter mice showed that the majority of CD8 cells (~94%) were positive for mCherry expression while all other immune cell subtypes (CD4, NKT, NK, B, macrophages, neutrophils, DCs) expressed minimal to no mCherry (~1%) (**Fig. S1D**).

MC38 colon carcinoma is highly responsive to radio-immunotherapy regimen

MC38 is a well-studied, immunologically hot tumor with high mutational burden.[72,73] CD8-mCherry reporter mice bearing ~150 mm^3 intradermal[74] (I.D.) flank MC38 tumors were treated with external beam radiation therapy, αCTLA-4, and IL-2 (**Fig. 1A**). Our radio-immunotherapy combination induced complete responses in 91% of treated mice (**Fig. 1B-C**) and significantly increased survival (**Fig. 1D**). When cured mice were rechallenged with a second MC38 tumor they cleared 100% of the rechallenged tumors while naïve mice cleared 0%, indicating this radio-immunotherapy produces a strong immune memory response (**Fig. 1E**). This radio-immunotherapy efficacy was also reproduced in C57BL/6J mice to ensure the response was not specific to our reporter mCherry mice (**Fig. S2A-D**).

Hot MC38 colon carcinoma cures are driven by CD8 T cells

To probe which immune cells are driving these radio-immunotherapy induced MC38 responses, we selectively depleted CD8, CD4, or NK cells. Radio-immunotherapy treated MC38-bearing mice depleted of CD4 or NK cells behaved no differently than treated mice receiving control IgG antibody – complete responses were observed in all mice (**Fig. 1F**). In contrast, radio-immunotherapy treated mice depleted of CD8 cells lost the ability to clear their tumors and responded similarly to mice that received radiation therapy alone but significantly different than αCD4, αNK, IgG groups (**Fig. 1F**). Thus, CD8 cells are critical for MC38 tumor response to our radio-immunotherapy *in vivo*. We further explored immune function during radio-immunotherapy using flow cytometry across treatment on days 0, 6, and 9. Gating strategies for all immune cell populations are in **Fig. S3A**. We showed that tumor infiltrating immune populations changed over time and with therapy, including a significant expansion of NK cells on day 6, a significant reduction of neutrophils on day 9, and a significant expansion of CD8 cells on day 9 (**Fig. 1G-H**, **S3B**). Functional measurements showed that CD8 cells from treated mice are more activated on day 6 versus day 9, as determined by CD69 expression (**Fig. 1I**), contain significantly higher granzyme B on both days, and express significantly higher levels of CD107a, a marker of degranulation, on day 6 compared to vehicle mice (**Fig. 1J**). In contrast, CD8 cells from treated mice express significantly less exhaustion markers compared to vehicle mice (**Fig. 1K**). As we saw a large expansion of NK cells during therapy, we also probed their functional changes. NK cells from treated mice were significantly more activated on day 6 (**Fig. 1L**) but showed no differences in effector function except for significantly increased degranulation (CD107a) on day 9 when compared to vehicle mice (**Fig. 1M**). NK cells from treated mice also expressed significantly less exhaustion markers compared to vehicle mice (**Fig. 1N**). CD4 cells from treated mice were significantly more activated on day 6 compared to day 9 treated mice (**Fig. S3C**), contained significantly higher perforin and granzyme B cytolytic granules, and expressed higher CD107a compared to vehicle mice (**Fig. S3D**). Like CD8 and NK cells, CD4 cells from treated mice expressed significantly less exhaustion markers compared to vehicle mice (**Fig. S3E**). In summary, antibody depletion experiments and functional flow cytometry across treatment time-course show that CD8 T cells drive MC38 tumor cures though some effector function is also observed within NK and CD4 T cell populations in this hot tumor.

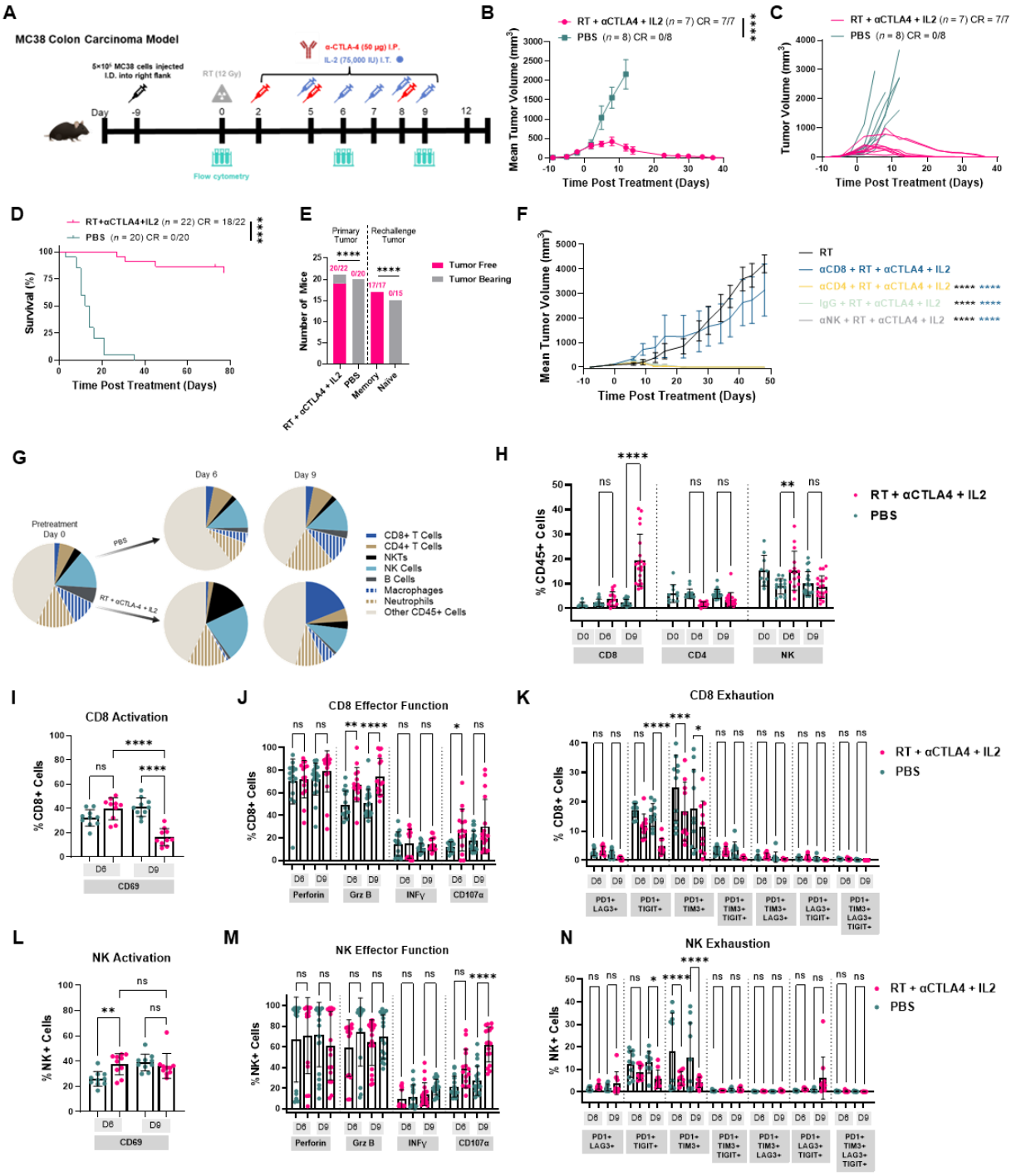

Figure 1. MC38 colon carcinoma response to radio-immunotherapy and immune cell role during cures.

A) Experimental timeline where flow cytometry was performed during therapy on day 0, 6, and 9. **B)** Mean tumor growth curves for treated and vehicle MC38-bearing mice (pairwise contrasts, *n* = 7-8 mice per group, mean ± SEM, 1 representative experiment shown, 3 experimental repeats). **C)** Individual tumor growth curves for treated and vehicle MC38-bearing mice (*n* = 7-8 mice per group, 1 representative experiment shown, 3 experimental repeats). **D)** Kaplan-Meier survival curve of treated and vehicle MC38-bearing mice (pairwise log-rank test, *n* = 20-22 mice per group, 3 experimental repeats combined). **E)** Number of tumor

free mice from treated and vehicle primary tumors and from treated and naïve tumor rechallenge (Fisher exact test, primary n = 20-22, rechallenge n = 15-17 mice per group, 3 experimental repeats). **F)** Mean tumor growth curves during CD8, CD4, and NK immune cell depletion of MC38-bearing mice (n = 5 mice per group, pairwise contrasts, 1 representative experiment shown, 2 experimental repeats, mean ± SEM). Note green, yellow, and gray curves are superimposed on the X axis. **G)** Flow cytometry of immune cell subsets in tumors from treated and vehicle MC38-bearing mice across treatment time (n = 5-10 mice per timepoint, 2 experimental repeats, % CD45+ cells). **H)** Flow cytometry of CD8, CD4, NK cell changes from treated and vehicle MC38-bearing mice across treatment time (one-way ANOVA, n = 5-10 mice per group, 2-3 experimental repeats, mean ± SD, % CD45+ cells). **I-K)** Flow cytometry of CD8 and **L-N)** NK activation, effector function, and exhaustion from treated and vehicle MC38-bearing mice across treatment time (n = 10-20 mice per group, one-way ANOVA, mean ± SD, % CD8+ or %NK+ cells, 2-4 experimental repeats) (*p < 0.05, **p < 0.01, ***p < 0.001, ****p < 0.0001).

In vivo imaging captures MC38 CD8 T cell metabolic dynamics from early glycolytic state to later memory state

We performed *in vivo* label-free OMI to track single CD8 T cell metabolic changes across treatment on days 0, 6, and 9 (**Fig. 2A**). Representative fluorescence intensity images showed increased CD8 infiltration and cell size (white outlines mark CD8 T cells) in treated mice versus vehicle mice (**Fig. 2B**, top row). Representative free NAD(P)H α_1 and protein-bound FAD α_1 images showed that CD8 T cell NAD(P)H and FAD protein-binding changes over treatment time-course (**Fig. 2B**, middle and bottom rows). Quantified single CD8 T cell metabolic changes showed an initial trend towards increased free NAD(P)H α_1 on day 6, suggesting a glycolytic shift in metabolism, followed by a significant decrease on day 9, suggesting an oxidative shift in metabolism (**Fig. 2C**). Furthermore, CD8 T cell metabolic changes showed a significant decrease in protein-bound FAD on day 6, also suggesting a glycolytic shift in metabolism, followed by an increase on day 9, also suggesting an oxidative shift in metabolism (**Fig. 2D**). Additionally, our metabolic imaging showed that CD8 T cell size increased on day 6, often correlated to T cell activation and proliferation, but not on day 9 (**Fig. 2E**). We trained a binary classifier on our CD8 T cell *in vivo* metabolic and size variables and tested if the algorithm could predict whether each CD8 T cell was from a treated or vehicle mouse tumor. On day 6, the classifier identified CD8 T cells from treated versus vehicle mice with high accuracy (area under the curve (AUC) = 0.94, **Fig. 2F**).

In vivo imaging captures MC38 tumor cell metabolic dynamics during radio-immunotherapy

We also captured single MC38 tumor cell metabolic changes across treatment on day 0, 6, and 9. Representative fluorescence intensity images showed changes in TME over time, with lower tumor density later in treatment (**Fig. 2B**, top row). Representative free NAD(P)H α_1 and protein-bound FAD α_1 images showed that MC38 tumor cell NAD(P)H and FAD protein-binding changes over treatment time-course (**Fig. 2B**, middle and bottom rows). Quantified single cell MC38 metabolic changes showed an initial, insignificant increase in free NAD(P)H α_1, suggesting a glycolytic shift in metabolism, on day 6 followed by a decrease on day 9, indicating an oxidative shift in metabolism (**Fig. 2G**). In contrast, MC38 tumor cell metabolic changes showed a decrease in protein-bound FAD on day 6, also suggesting a glycolytic shift in metabolism, with no change on day 9 (**Fig. 2H**). These metabolic shifts were validated by plating MC38 *in vitro* and applying known metabolic inhibitors including a glycolysis inhibitor, 2-Deoxy-D-glucose (2DG), and an electron transport chain complex IV inhibitor, sodium cyanide (NaCN) (**Fig. S4**). We trained a binary classifier on *in vivo* MC38 tumor cell metabolic variables and tested sensitivity to treatment vs. vehicle condition. On day 6, the classifier identified MC38 tumor cells from treated versus vehicle mice with very high accuracy (AUC = 0.98, **Fig. 2I**).

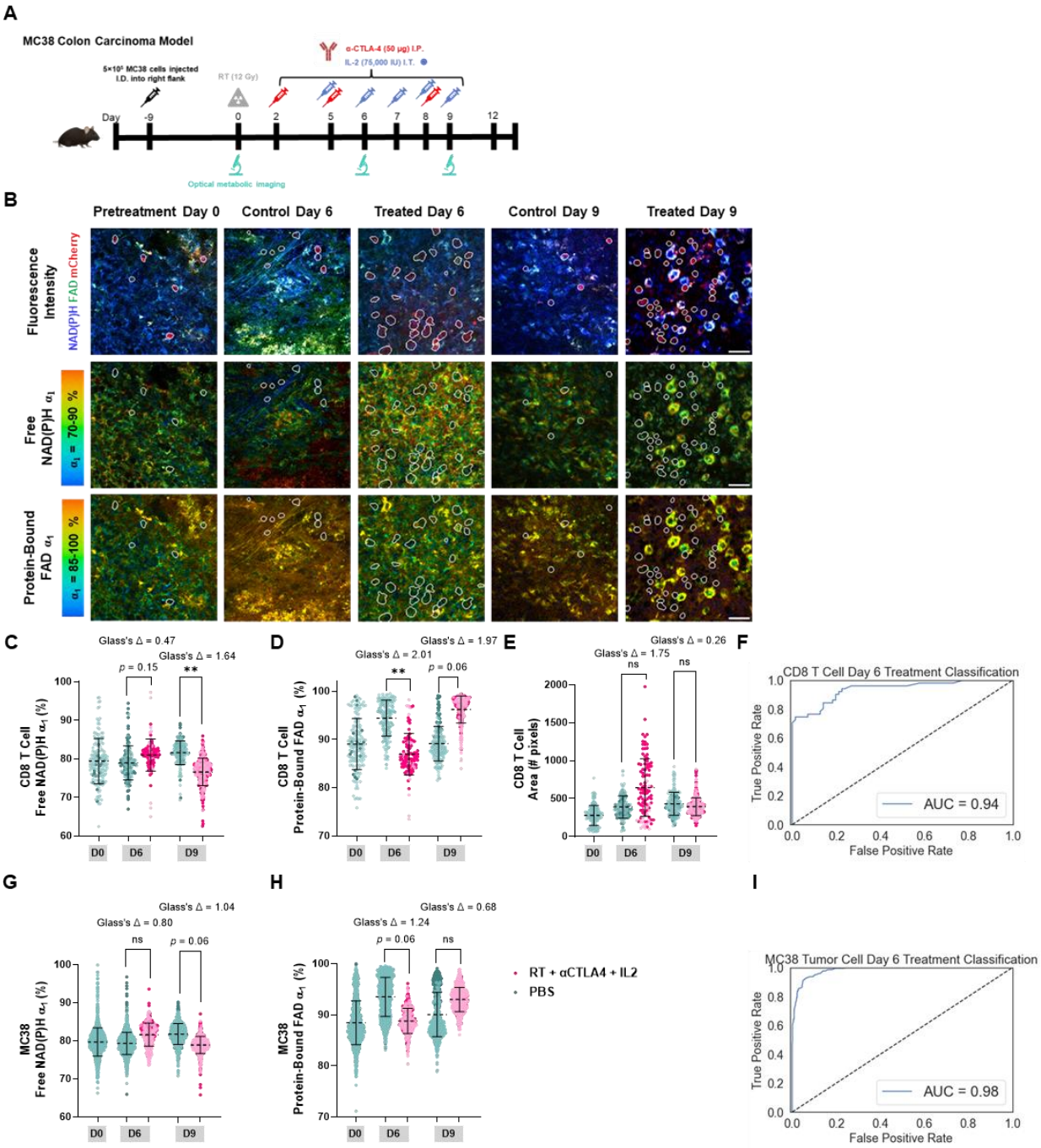

Figure 2. *In vivo* fluorescence intensity and lifetime imaging of CD8 T cells in MC38 colon carcinoma tumors shows metabolic co-enzyme protein-binding changes with treatment.

A) Experimental timeline where *in vivo* OMI was performed during therapy on day 0, 6, and 9. **B)** Representative *in vivo* MC38 colon carcinoma tumor images across time. Fluorescence intensity images (top row) show infiltrating CD8 T cells (red) expressing mCherry and autofluorescent NAD(P)H (blue) and FAD (green) present in all cells. NAD(P)H α_1 (middle row) and FAD α_1 (bottom row) images show spatial distribution of metabolic changes within the tumors. CD8 T cell outlines (white) overlaid on all images for clarity (1 experiment shown, 2 experimental repeats performed, scale bar 50 μm). **C)** Quantified CD8 T cell free NAD(P)H (α_1) changes during therapy. **D)** Quantified CD8 T cell protein-bound FAD (α_1) changes during therapy. **E)** Quantified CD8 T cell area changes during therapy. **F)** Receiver operating characteristic

(ROC) curve (area under the curve (AUC) = 0.94) classifying treated or vehicle CD8 T cells from day 6. **G)** Quantified MC38 tumor cell free NAD(P)H (α_1) changes during therapy. **H)** Quantified MC38 tumor cell protein-bound FAD (α_1) changes during therapy. **I)** ROC curve (AUC = 0.98) classifying treated or vehicle MC38 tumor cells from treatment day 6. **C-E)** *n* = 4 mice per day, *n* = 2-4 mice per group, Day 0 *n* = 152 cells, Day 6 *n* = 244 cells, Day 9 *n* = 469 cells, CD8 T cells imaged, mixed-effects ANOVA and Glass's Δ, mean ± SD, 2 experimental repeats. **G-H)** *n* = 4 mice per day, *n* = 2-4 mice per group, Day 0 *n* = 1445 cells, Day 6 *n* = 1882 cells, Day 9 *n* = 1409 cells, MC38 tumor cells imaged, mixed-effects ANOVA and Glass's Δ, mean ± SD, 2 experimental repeats. **F, I)** Random Forest algorithm, 50% train: 50% test, **Table S1** shows 9 variables included, day 0 data not included.

B78 melanoma responsive to radio-immunotherapy regimen

Next, we transitioned to a difficult to treat, immunologically cold B78 melanoma tumor. CD8-mCherry reporter mice bearing I.D. ~150mm^3 flank B78 tumors were treated with radiation therapy, αCTLA-4, and Hu14.18-IL2 immunocytokine (**Fig. 3A**). Our radio-immunotherapy combination induced complete responses in 58% of treated mice (**Fig. 3B-C, E**) and significantly increased survival (**Fig. 3D**). When cured mice were rechallenged with a second B78 tumor without additional therapy, they cleared 80% of the rechallenged tumors while naïve mice cleared 0%, indicating this radio-immunotherapy produces a strong immune memory response (**Fig. 3E**). This radio-immunotherapy efficacy was also reproduced in C57BL/6J mice to ensure the response was not specific to our reporter mCherry mice (**Fig. S2E-H**).

Cold B78 melanoma cures driven by CD4 T cells

Recently we showed that mice bearing smaller B78 tumors (~50 mm^3) that can be cured with RT and Hu14.18-IL2 alone require CD4 T cells to achieve effective cures and memory responses, but NK and CD8 T cells are not required.[19] To probe which immune cells are driving the B78 responses and producing the immune memory in these larger tumors when αCTLA-4 is included with RT and Hu14.18-IL2, we performed immune depletion studies where we selectively depleted CD8, CD4, or NK cells during therapy. B78-bearing mice depleted of CD8 or NK cells behaved similarly to mice treated with IgG antibody alone – potent tumor growth inhibition was seen in all 3 of these groups (**Fig 3F**) and complete responses were observed in 40-70% of these mice. In contrast, B78-bearing mice depleted of CD4 cells lost the ability to clear their tumors and responded no differently than mice that received PBS alone but significantly different than αCD8, αNK, IgG groups (**Fig. 3F**). Similar to what we observed with RT and Hu14.18-IL2 alone in smaller B78 tumors,[19] this work highlights that CD4 cells are critical for B78 tumor response to our radio-immunotherapy *in vivo*. We further explored immune function during our combination therapy using flow cytometry across treatment time. We showed that the tumor infiltrating immune populations changed over time and with therapy including a significant expansion of CD8 cells on days 9 and 12, a significant reduction in macrophages on days 9 and 12, and a significant expansion of neutrophils on day 12 (**Fig. 3G-H**, **S3F**). Functional measurements showed that CD8 cells from treated mice are significantly activated on day 6 (**Fig. 3I**), contain significantly higher granzyme B on days 6 and 12, but express minimal to no CD107a (**Fig. 3J**). These data are consistent with what we observed in smaller B78-bearing mice with RT and Hu14.18-IL2 alone.[19] Additionally, CD8 cells from treated mice express significantly higher exhaustion markers compared to vehicle mice (**Fig. 3K**). In comparison, CD4 cells from treated mice were significantly more activated on day 6 (**Fig. 3L**), contained significantly higher granzyme B on day 6, and expressed some CD107a (~5%) though it was not significantly different than vehicle mice (**Fig. 3M**). CD4 cells from treated mice also expressed significantly less exhaustion markers compared to vehicle mice (**Fig. 3N**). NK cells from treated mice were significantly more activated on day 6 and 12 (**Fig. S3G**) and contained significantly higher perforin and granzyme B on day 6 and 12, though minimal to no CD107a was expressed (**Fig. S3H**). NK cells from treated mice expressed low levels of exhaustion markers overall though a few were significantly higher than vehicle mice (**Fig. S3I**). In summary, antibody depletion experiments and functional flow cytometry show CD4 T cells drive B78 tumor cures across treatment time, presumably through some effector function but maybe helper function. CD8 T cells are not critical to tumor cures. Though CD8 T cells do become activated and express cytotoxic granules, no direct killing is observed (no degranulation via CD107a) and exhaustion markers are high with treatment.

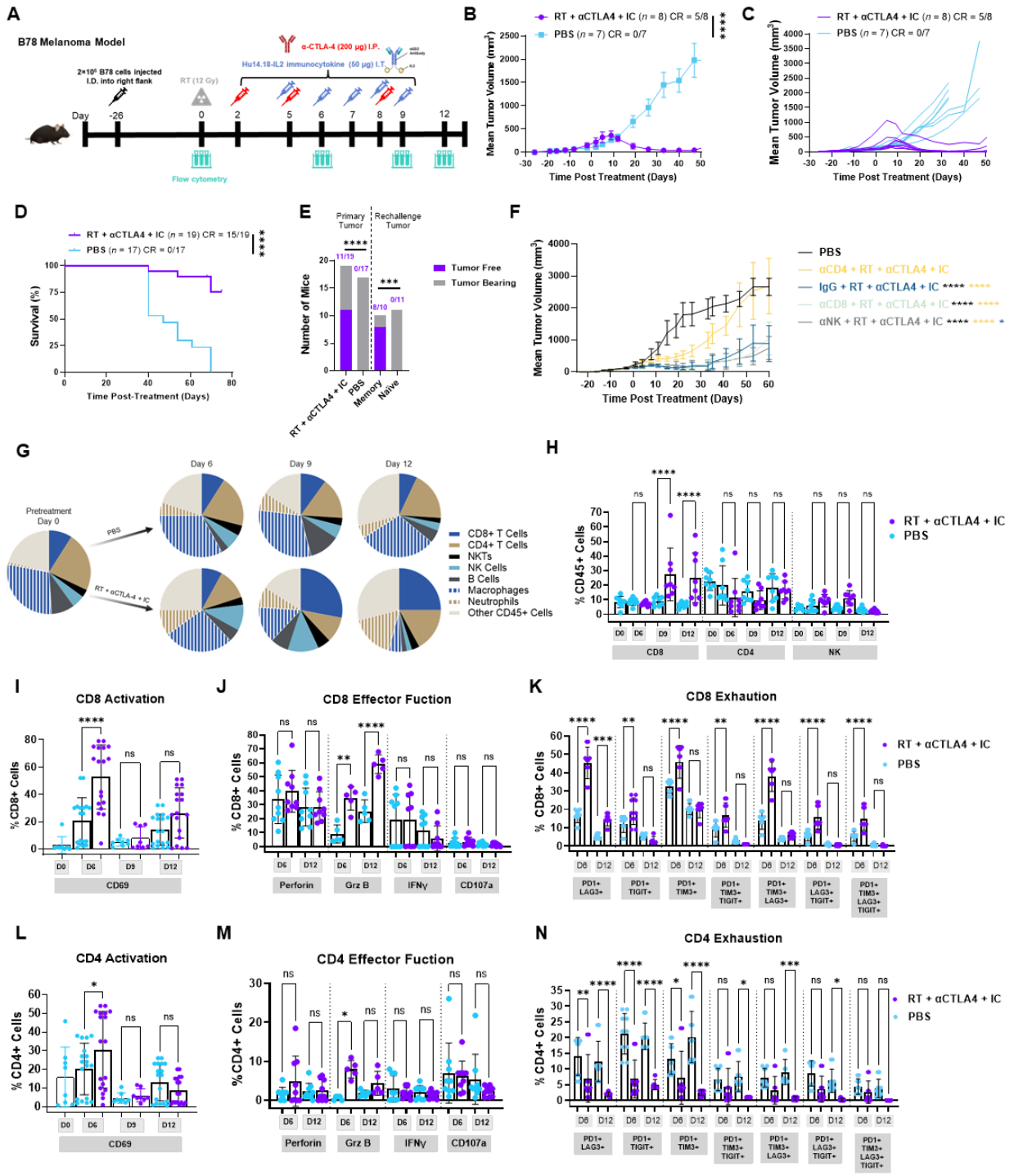

Figure 3. Radio-immunotherapy regimen leads to durable responses and immune infiltrate changes in B78 melanoma model.

A) Experimental timeline where flow cytometry was performed during therapy on day 0, 6, 9, and 12. **B)** Mean tumor growth curves for treated and vehicle B78-bearing mice (pairwise contrasts, *n* = 7-8 mice per group, mean ± SEM, 1 representative experiment shown, 3 experimental repeats). **C)** Individual tumor growth curves for treated and vehicle B78-bearing mice (*n* = 7-8 mice per group, 1 representative experiment shown, 3 experimental repeats). **D)** Kaplan-Meier survival curve of treated and vehicle B78-bearing mice (pairwise log-rank test, *n* = 17-19 mice per group, 3 experimental repeats combined). **E)** Number of tumor free mice from treated and vehicle primary tumors and from treated and naïve tumor

rechallenge (Fisher exact test, primary *n* = 17-19, rechallenge *n* = 10-11 mice per group, 3 experimental repeats). **F)** Mean tumor growth curves during CD8, CD4, and NK immune cell depletion for B78-bearing mice (*n* = 10 mice per group, pairwise contrasts, 1 experimental replicate, mean ± SEM). **G)** Flow cytometry of immune cell subsets in tumors from treated and vehicle B78-bearing mice across treatment time (*n* = 8 mice per day, 2 experimental repeats, % CD45+ cells). **H)** Flow cytometry of CD8, CD4, NK cell changes from treated and vehicle B78-bearing mice across treatment time (*n* = 10 mice per group, one-way ANOVA, 2 experimental repeats, mean ± SD). **I-K)** Flow cytometry of CD8 and **L-N)** CD4 T cell activation, effector function, and exhaustion from treated and vehicle B78-bearing mice across treatment time (*n* = 8-18 mice per group, one-way ANOVA, mean ± SD, % CD8+ or % CD4+ cells, 2-4 experimental repeats).

In vivo imaging captures B78 CD8 T cell atypical metabolic dynamics, with no glycolytic shift observed

To further understand why CD8 T cells are not functional in this cold B78 model, we performed *in vivo* label-free OMI to track single CD8 T cell metabolic changes across treatment on day 0, 6, 9, and 12 (**Fig. 4A**). Representative fluorescence intensity images showed decreased CD8 T cell infiltration (white outlines mark CD8 T cells) in treated mice versus vehicle mice, especially at day 6 and 9 (**Fig. 4B**, top row). Representative free NAD(P)H α_1 and protein-bound FAD α_1 images showed that CD8 T cell NAD(P)H and FAD protein-binding changes are minimal over treatment time-course (**Fig. 4B**, middle and bottom rows). Quantified single cell CD8 T cell metabolic changes showed no significant changes in free NAD(P)H α_1 on any days, though Glass's Δ indicated a trend towards decreased free NAD(P)H or oxidative metabolism shift (**Fig. 4C**). CD8 T cell metabolic changes showed an increase in protein-bound FAD on day 9 only, indicating an oxidative metabolism shift (**Fig. 4D**). Despite the minimal metabolic changes, our imaging showed that CD8 T cell size significantly increased on day 6 with an increasing trend on day 9 (**Fig. 4E**). We trained a binary classifier on CD8 T cell *in vivo* metabolic and size variables and tested sensitivity to treated vs. vehicle condition. On day 9, the classifier identified CD8 T cells from treated versus vehicle mice with high accuracy (AUC = 0.90, **Fig. 4F**).

In vivo imaging captures B78 tumor cell metabolic dynamics during radio-immunotherapy

We also captured single B78 tumor cell metabolic changes across treatment time-course on day 0, 6, 9, and 12. Representative fluorescence intensity images showed changes in TME over time with fewest CD8 T cells present on day 6 and lower tumor cell density later in treatment (**Fig. 4B**, top row). Representative free NAD(P)H α_1 and protein-bound FAD α_1 images showed that B78 tumor cell NAD(P)H and FAD mean protein-binding minimally change over treatment time-course though heterogeneity was observed throughout regions of the tumors (**Fig. 4B**, middle and bottom rows). Quantified single cell B78 metabolic changes showed no changes in free NAD(P)H α_1 on any treatment day (**Fig. 4G**). B78 tumor cell metabolic changes showed an increase in protein-bound FAD on day 9 only, indicating a shift towards oxidative metabolism (**Fig. 4H**). These metabolic shifts were validated by plating B78 *in vitro* and applying known metabolic inhibitors including a glycolysis inhibitor 2DG, and an electron transport chain inhibitor, NaCN (**Fig. S5**). We trained a binary classifier on B78 tumor cell *in vivo* metabolic variables and tested sensitivity to treated vs vehicle condition. On day 9, the classifier identified B78 tumor cells from treated versus vehicle mice with modest accuracy (AUC of ROC = 0.85, **Fig. 4I**).

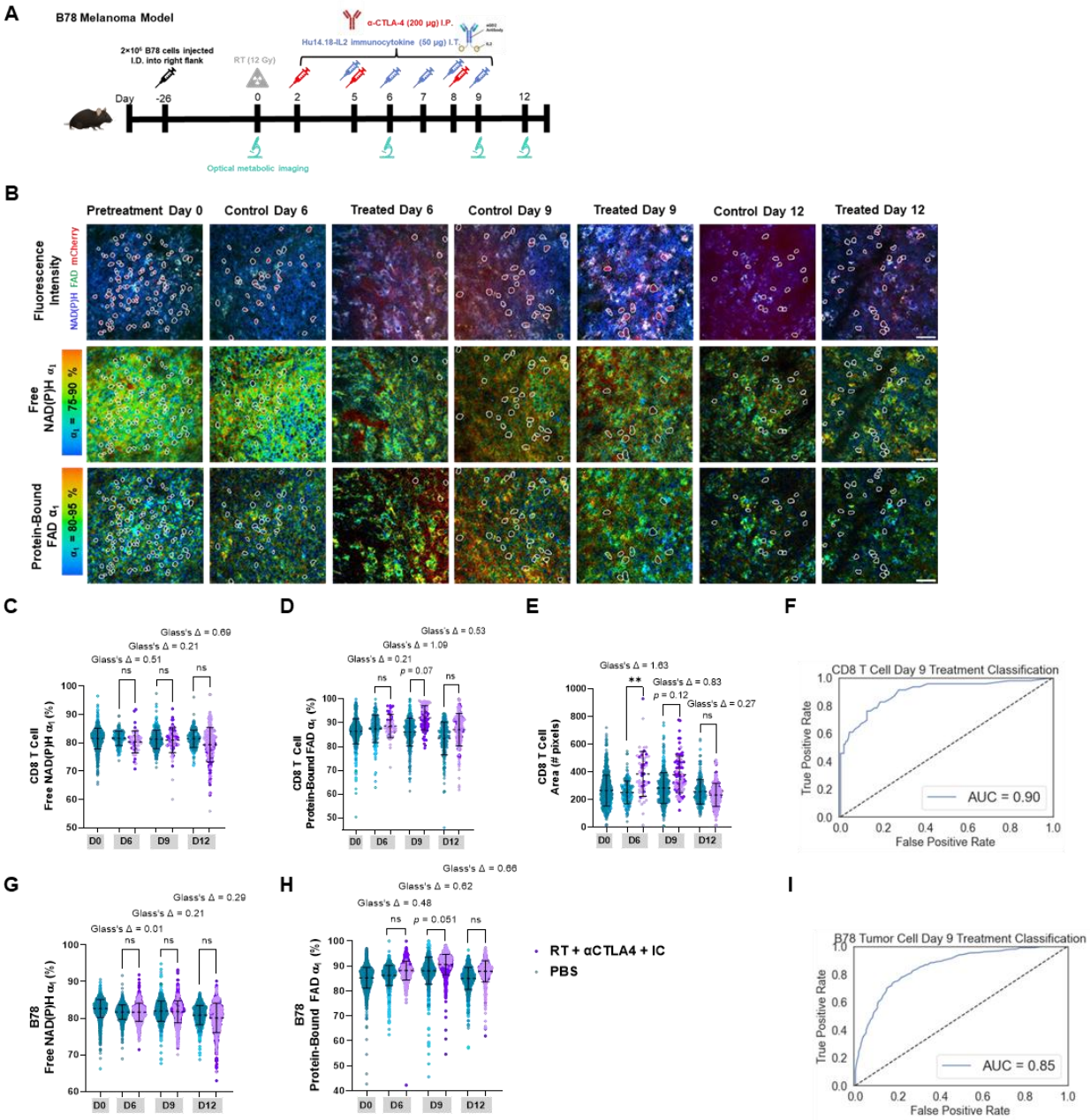

Figure 4. *In vivo* fluorescence intensity and lifetime imaging of CD8 T cells and B78 melanoma tumors shows metabolic co-enzyme protein-binding changes with treatment.

A) Experimental timeline where *in vivo* OMI was performed during therapy on day 0, 6, 9, and 12. **B)** Representative *in vivo* B78 melanoma tumor images across time. Fluorescence intensity images (top row) show infiltrating CD8 T cells (red) expressing mCherry and autofluorescent NAD(P)H (blue) and FAD (green) present in all cells. NAD(P)H α_1 (middle row) and FAD α_1 (bottom row) images show spatial distribution of metabolic changes within the tumors. CD8 T cell outlines (white) overlaid on all images for clarity (1 experiment shown, 2 experimental repeats performed, scale bar 50 μm). **C)** Quantified CD8 T cell free NAD(P)H (α_1) changes during therapy. **D)** Quantified CD8 T cell protein-bound FAD (α_1) changes during therapy. **E)** Quantified CD8 T cell area changes during therapy. **F)** ROC curve (AUC = 0.90) classifying treated or vehicle CD8 T cells from day 9. **G)** Quantified B78 tumor cell free NAD(P)H (α_1) changes during therapy. **H)** Quantified B78 tumor cell protein-bound FAD (α_1) changes during therapy. **I)** ROC curve (AUC = 0.85) classifying treated or vehicle B78 tumor cells from treatment day 9. **C-E)** n = 4

mice per day, *n* = 2-4 mice per group, Day 0 *n* = 794 cells, Day 6 *n* = 247 cells, Day 9 *n* = 463 cells, Day 12 *n* = 438 cells, CD8 T cells imaged, mixed-effects ANOVA and Glass's Δ, mean ± SD, 2 experimental repeats. **G-H)** *n* = 4 mice per day, *n* = 2-4 mice per group, Day 0 *n* = 2587 cells, Day 6 *n* = 2521 cells, Day 9 *n* = 2203 cells, Day 12 *n* = 1841 cells, B78 tumor cells imaged, mixed-effects ANOVA and Glass's Δ, mean ± SD, 2 experimental repeats. **F, I)** Random Forest algorithm, 50% train: 50% test, **Table S1** shows 8 variables included, day 0 data not included.

scRNAseq confirms B78 CD8 T cell metabolic gene expression changes with radio-immunotherapy

Next, using single cell RNA sequencing (scRNAseq) data generated from our previous work in B78-bearing mice,[19] we asked how metabolism-related gene expression changes at the single cell level for CD8 T cells during radio-immunotherapy to corroborate our *in vivo* metabolic imaging findings. In that study, C57BL/6 mice bearing I.D. flank B78 tumors were treated with external beam radiation therapy and Hu14.18-IL2 immunocytokine only and tumors were harvested and processed for scRNAseq on Day 8 (**Fig. 5A**).[19] Within the CD45+ cell population, CD8 T, CD4 T, and NK cells were identified and clustered by treatment group. CD8 T, CD4 T, and NK cells from treated mice were overall more metabolically active, with increased gene expression from several KEGG[75–77] metabolism pathways (**Fig. 5B-C**). CD8 cells from treated mice most upregulated metabolic genes related to oxidative phosphorylation with additional immune function implicated by upregulation in genes related to antigen processing/presentation (**Fig. 5C**). In contrast, CD4 cells from treated mice most upregulated metabolic genes related to arginine and proline metabolism while NK cells most upregulated metabolic genes related to glycine/serine/threonine metabolism (**Fig. 5C**). Within CD8 T cells, we observed striking cellular heterogeneity differences between treated and vehicle mice including reduction of subset 1 and expansion of subsets 2-6 in treated mice (**Fig. 5D**) where subsets 1 and 4 lowly expressed genes in KEGG metabolism pathways in both treated and vehicle mice (**Fig. 5E**). While subsets 2 and 3 showed minimal change, subsets 5 and 6 showed the highest metabolic activity gene expression with treatment including an upregulation of genes related to pentose phosphate pathway and glycolysis/gluconeogenesis (subset 5) and glycolysis/gluconeogenesis, pentose phosphate pathway, oxidative phosphorylation, pyruvate metabolism, and fatty acid metabolism within subset 6 (**Fig. 5E**). These subsets expressed genes related to DNA repair and chromatin activity (*Rrm1*, *Hist1h2am*, *Hist1h2ae*, *Hist1h1b*, *Top2a*, *Pclaf*), mitosis (*Spc24*, *Cks1b*, *Smc1*), proliferation and apoptosis suppression (*Mki67*, *Birc5*), and chemotaxis (*Xcl1*), and expressed cytotoxic and stem-like gene signatures (**Fig. 5F, H**). Furthermore, subsets 1 and 2 expressed significantly higher gene expression of glycolytic genes (*Gpi1, Pgm2*) while subsets 5 and 6 expressed significantly higher gene expression of oxidative genes (*Ndufa13*, *Cox6a1*) (**Fig. 5G**). To complement the metabolic characterization of the CD8 subsets, we also examined KEGG immune functional pathways (**Fig. 5I**). Similarly to the KEGG metabolism changes, we observed that subsets 5 and 6 exhibited enhanced functionality after treatment, including increased T cell receptor (TCR) signaling and IL-17 signaling signatures (subset 5) and FCε RI signaling and IL-17 signaling signatures (subset 6) **(Fig. 5I)**. In summary, gene expression changes related to metabolism and immune function indicated CD8 T cells are phenotypically changed in treated mice.

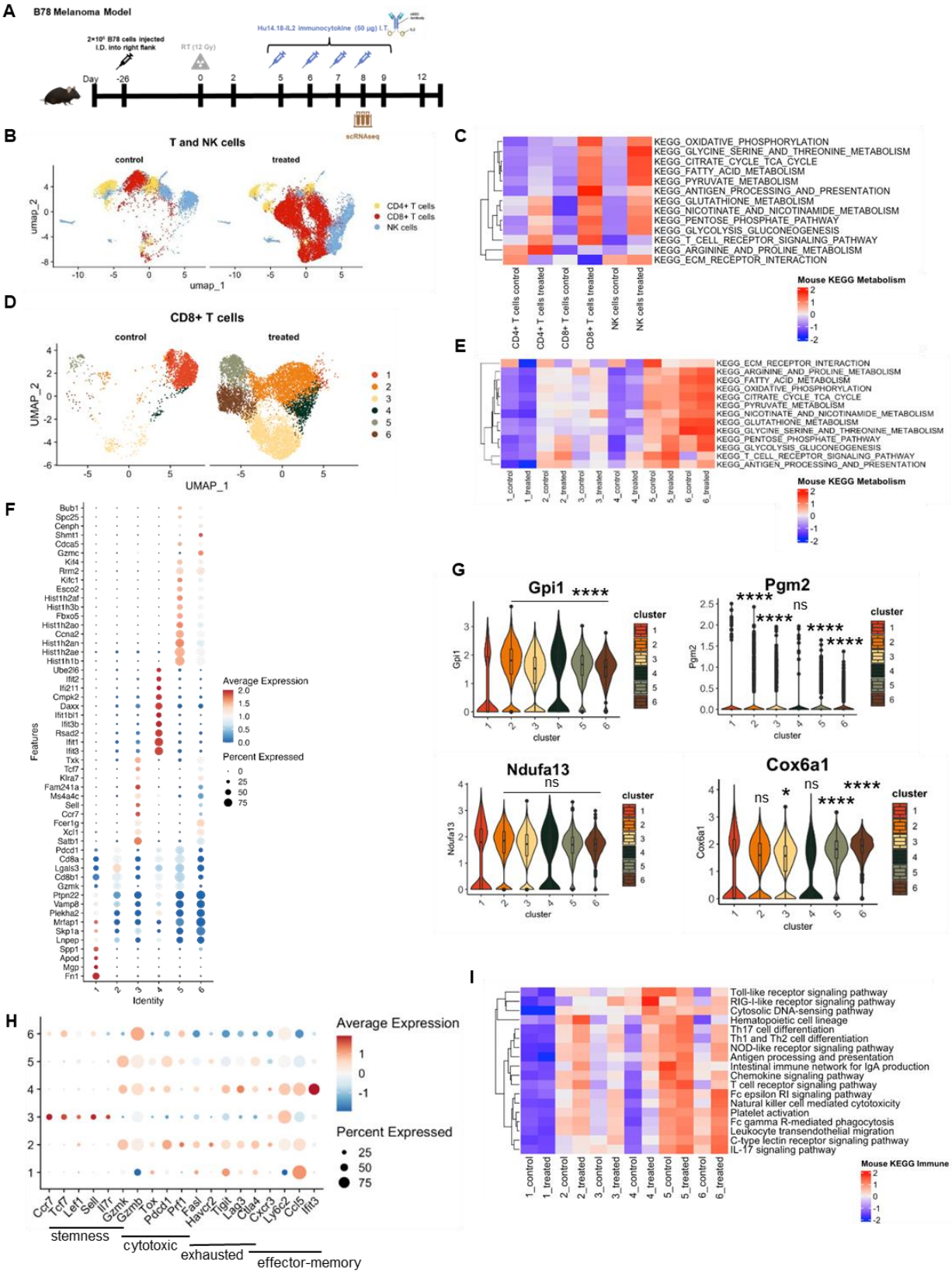
A
B78 Melanoma Model
2×10⁶ B78 cells injected I.D. into right flank
RT (12 Gy)
Hu14.18-IL2 immunocytokine (50 µg) I.T.
Day -26 0 2 5 6 7 8 9 12
scRNAseq
B
T and NK cells
control
treated
umap_2
umap_1
CD4+ T cells
CD8+ T cells
NK cells
C
KEGG_OXIDATIVE_PHOSPHORYLATION
KEGG_GLYCINE_SERINE_AND_THREONINE_METABOLISM
KEGG_CITRATE_CYCLE_TCA_CYCLE
KEGG_FATTY_ACID_METABOLISM
KEGG_PYRUVATE_METABOLISM
KEGG_ANTIGEN_PROCESSING_AND_PRESENTATION
KEGG_GLUTATHIONE_METABOLISM
KEGG_NICOTINATE_AND_NICOTINAMIDE_METABOLISM
KEGG_PENTOSE_PHOSPHATE_PATHWAY
KEGG_GLYCOLYSIS_GLUCONEOGENESIS
KEGG_T_CELL_RECEPTOR_SIGNALING_PATHWAY
KEGG_ARGININE_AND_PROLINE_METABOLISM
KEGG_ECM_RECEPTOR_INTERACTION
CD4+ T cells control
CD4+ T cells treated
CD8+ T cells control
CD8+ T cells treated
NK cells control
NK cells treated
Mouse KEGG Metabolism
D
CD8+ T cells
control
treated
UMAP_2
UMAP_1
E
1_control
1_treated
2_control
2_treated
3_control
3_treated
4_control
4_treated
5_control
5_treated
6_control
6_treated
F
Features
Identity
Average Expression
Percent Expressed
G
Gpi1
Pgm2
Ndufa13
Cox6a1
cluster
ns
H
Average Expression
Percent Expressed
Ccr7
Tcf7
Lef1
Sell
Il7r
Gzmk
Gzmb
Tox
Pdcd1
Prf1
Fasl
Havcr2
Tigit
Lag3
Ctla4
Cxcr3
Ly6c2
Ccl5
Ifit3
stemness
cytotoxic
exhausted
effector-memory
I
Toll-like receptor signaling pathway
RIG-I-like receptor signaling pathway
Cytosolic DNA-sensing pathway
Hematopoietic cell lineage
Th17 cell differentiation
Th1 and Th2 cell differentiation
NOD-like receptor signaling pathway
Antigen processing and presentation
Intestinal immune network for IgA production
Chemokine signaling pathway
T cell receptor signaling pathway
Fc epsilon RI signaling pathway
Natural killer cell mediated cytotoxicity
Platelet activation
Fc gamma R-mediated phagocytosis
Leukocyte transendothelial migration
C-type lectin receptor signaling pathway
IL-17 signaling pathway
Mouse KEGG Immune

Figure 5. B78 immune cell scRNAseq highlights metabolic gene expression changes during radio-immunotherapy.
A) Experimental timeline where single cell RNA sequencing was performed during therapy on day 8**. B)** UMAP projection of T and NK cells from treated and vehicle B78-bearing mice. **C)** Heatmap of CD8, CD4, and NK KEGG metabolism average gene expression changes within treated and vehicle B78-bearing mice. **D)** UMAP projection of CD8 T cell subsets from treated and vehicle B78-bearing mice. **E)** Heatmap of CD8 KEGG metabolism average gene expression changes from treated and vehicle B78-bearing mice. **F)** Dot Plot of top 10 genes expressed by each CD8 T cell subset (6 subsets) from treated and vehicle B78-bearing mice. **G)** Quantified gene expression changes for glycolysis-associated genes (*Gpi1*, *Pgm2*) and oxidative phosphorylation-associated genes (*Ndufa13*, *Cox6a1*) across CD8 T cell subsets from treated and vehicle B78-bearing mice (Wilcoxon rank-sum test with Benjamini-Hochberg correction). **H)** Dot Plot of CD8 T cell phenotypes across cell subsets from treated and vehicle B78-bearing mice. **I)** Heatmap of CD8 KEGG immune function average gene expression changes within treated and vehicle B78-bearing mice.
B-I) *n* = 2 mice per treatment group, 1 experimental replicate.

scRNAseq analysis of B78 tumors showss tumor metabolic shifts linked to radio-immunotherapy

We also reanalyzed the GD2+ B78 tumor cell populations within our scRNAseq data[19] (**Fig. 6A**) and asked if there were metabolic changes in the gene expression of the tumor cells. We observed that *Sox10* expressing tumor cells from vehicle and treated mice are largely different when two major tumor clusters were selected from the scRNAseq analysis (**Fig. 6B**). Tumors from vehicle mice expressed upregulated genes related to cell proliferation/motility/invasion (*Gpc3*, *Tspan13*, *Ccpg1*, *Asah1, Itfg1*), metabolism (*Cyp20a1*, *Aldoc*), enzymes that degrade gangliosides (*Hexb*), inhibition of apoptosis and promotion of angiogenesis (*Srpx2*, *Capn6*), promotion of fibroblasts and collagen deposition (*Glg1*, *Fmod*), and others (subset 0) (**Fig. 6C**). On the other hand, tumors from treated mice upregulated genes related to both inhibition (*Ifit3*, *Ifit3b*) and promotion (*Xaf1*) of apoptosis, increased PD-L1 expression (*Cd274*), increased GTPase activity tied to cell signaling/proliferation/migration/cytoskeletal organization (*Gbp6*, *Tgtp1*, *Irgm1*, *Iigp1*, *Igtp*, *Gbp3*, *Gbp2*), and interferon signaling (*Ifi47*, *Apol9b*) (subset 1) (**Fig. 6C**). KEGG metabolism pathway signatures are distinct between the two subsets, where subset 0 showed a downregulation of metabolic genes and activity in the treated mice versus high arginine / proline metabolism within the vehicle mice (**Fig. 6D**). Subset 1 from treated mice also showed a downregulation of most metabolic genes and activity versus vehicle except for increased nicotinate / nicotinamide metabolism (**Fig. 6D**). In contrast, subset 1 from the vehicle mice expressed an increase in genes related to glycine / serine / threonine metabolism, glutathione metabolism, and citrate cycle / TCA cycle (**Fig. 6D**). Focusing on two glycolysis related genes (*Gpi1, Pgam1*) and two oxidative phosphorylation genes (*Sdha, Cox15*) we observed that subset 0 expressed significantly higher gene expression of glycolytic genes while subset 1 expressed significantly higher gene expression of one of the oxidative genes (**Fig. 6E**). We also observed an upregulation in genes associated with apoptosis within tumor subset 1 (**Fig. 6F**). In summary, we observed that B78 tumor cells from vehicle mice versus treated mice have distinct gene expression in metabolism and related functions based on scRNAseq.

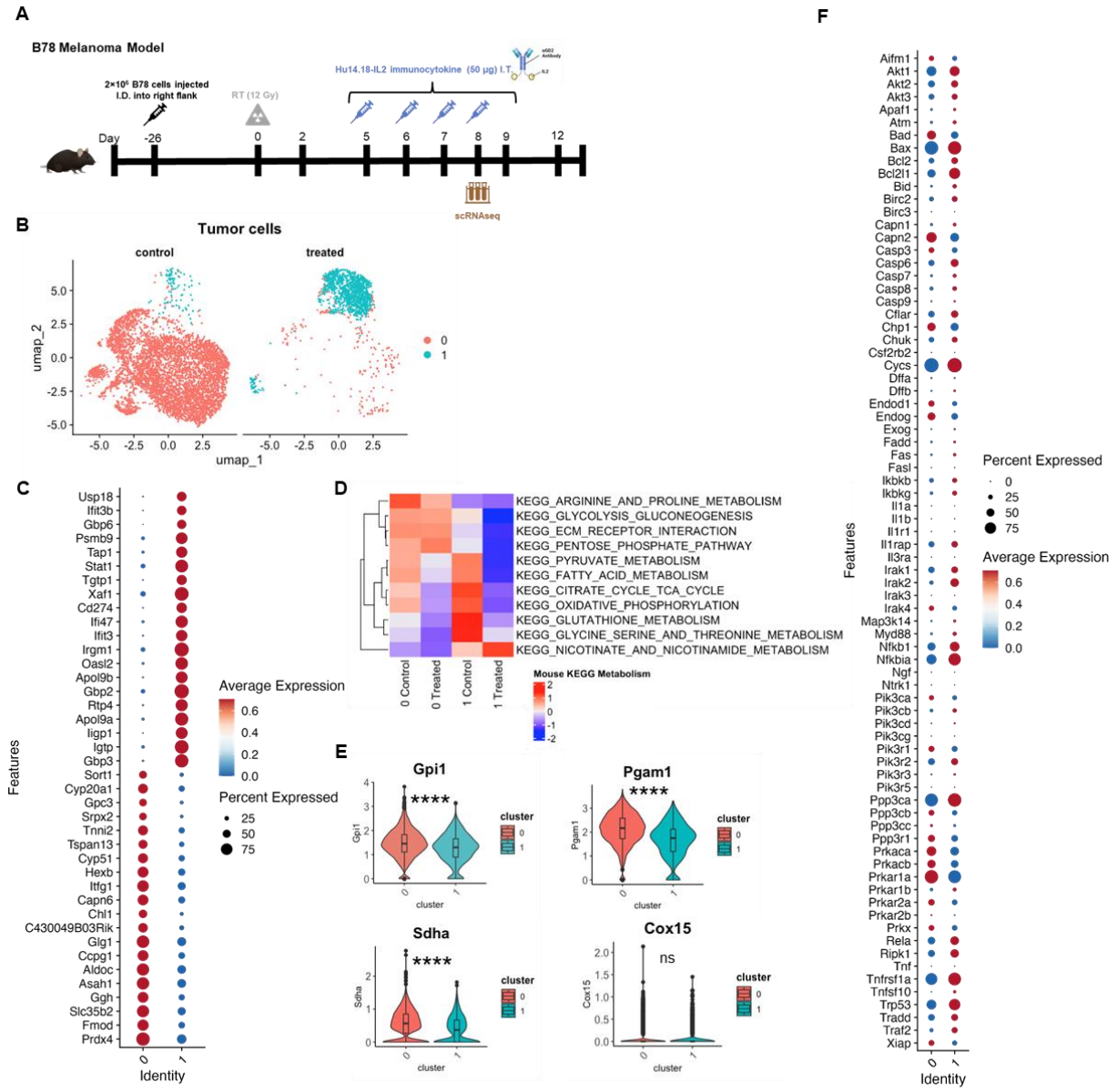

Figure 6. B78 tumor cell scRNAseq highlights tumor metabolic gene expression changes during radio-immunotherapy

A) Experimental timeline where single cell RNA sequencing was performed during therapy on day 8**. B)** UMAP projection of B78 tumor cells from treated and vehicle B78-bearing mice. **C)** Dot Plot of top 20 genes expressed by each B78 tumor cell subset (2 subsets) from treated and vehicle B78-bearing mice. **D)** Heatmap of B78 KEGG metabolism average gene expression changes from treated and vehicle B78-bearing mice. **E)** Quantified gene expression changes for glycolysis-associated genes (*Gpi1*, *Pgm2*) and oxidative phosphorylation-associated genes (*Sdha*, *Cox15*) across B78 tumor cell subsets from treated and vehicle B78-bearing mice (Wilcoxon rank-sum test with Benjamini-Hochberg correction). **F)** Dot Plot of top 40 KEGG apoptosis genes for each B78 tumor cell subset from treated and control B78-bearing mice.
B-F) *n* = 2 mice per treatment group, 1 experimental replicate.

Multiplex immunofluorescence spatial profiling of B78 tumor and lymph node elucidates infiltration changes and immune-tumor interactions with radio-immunotherapy

Finally, we performed multiplex immunofluorescence on B78 tumors and lymph nodes harvested from treated and vehicle mice on days 0, 6, 9, and 12 (**Fig. 7A**). Tumors were stained for cell nuclei (DAPI), immune cells (CD4, CD8α, CD161), tumor cells (SOX10), cytotoxic granules (perforin), and cell death (cPARP-1) (**Fig. 7B, Fig. S6A**). Representative tumor regions of interest (ROI) across treatment time showed changes in immune infiltration, tumor organization, and cell death (**Fig. 7B, Fig. S6A**). Tumor ROI from treated mice showed significantly increased CD8 and CD4 T cell infiltration on Day 12 as well as significantly decreased SOX10 tumor cells on Day 12 (**Fig. 7C-E**) while perforin significantly increased on Day 6 (**Fig. S6B**). Spatial profiling via distance ratio from CD4 cells to nearest SOX10+ tumor cell revealed that CD4 cells were originally farther away in treated mice on Day 6 but then transitioned to being closer to tumor cells on Days 9 and 12, compared to vehicle mice (**Fig. 7F**). In contrast, the distance ratio from CD8 cells to nearest SOX10+ tumor cell showed that on Day 6, CD8 cells from treated and vehicle mice were the same distance away from tumor but then with treatment, CD8 cells transitioned to being closer to tumor cells on Days 9 and 12 (**Fig. 7G**). Tumor draining lymph nodes were stained for cell nuclei (DAPI), immune cells (CD3, CD4, CD8α, CD19, F4/80), and cell activation (CD69) (**Fig. 7H, Fig. S6D-E**). Lymph node images from treated mice showed increased numbers of B cells as well as CD4 and CD8 T cells on Days 9 (peak) and 12 compared to vehicle mice (**Fig. 7I-K**), suggesting immune priming and activation is more robust in treated mouse lymph nodes. This is consistent with what we observe in the tumor draining lymph nodes of mice treated with RT and Hu14.18-IL2 alone.[19]

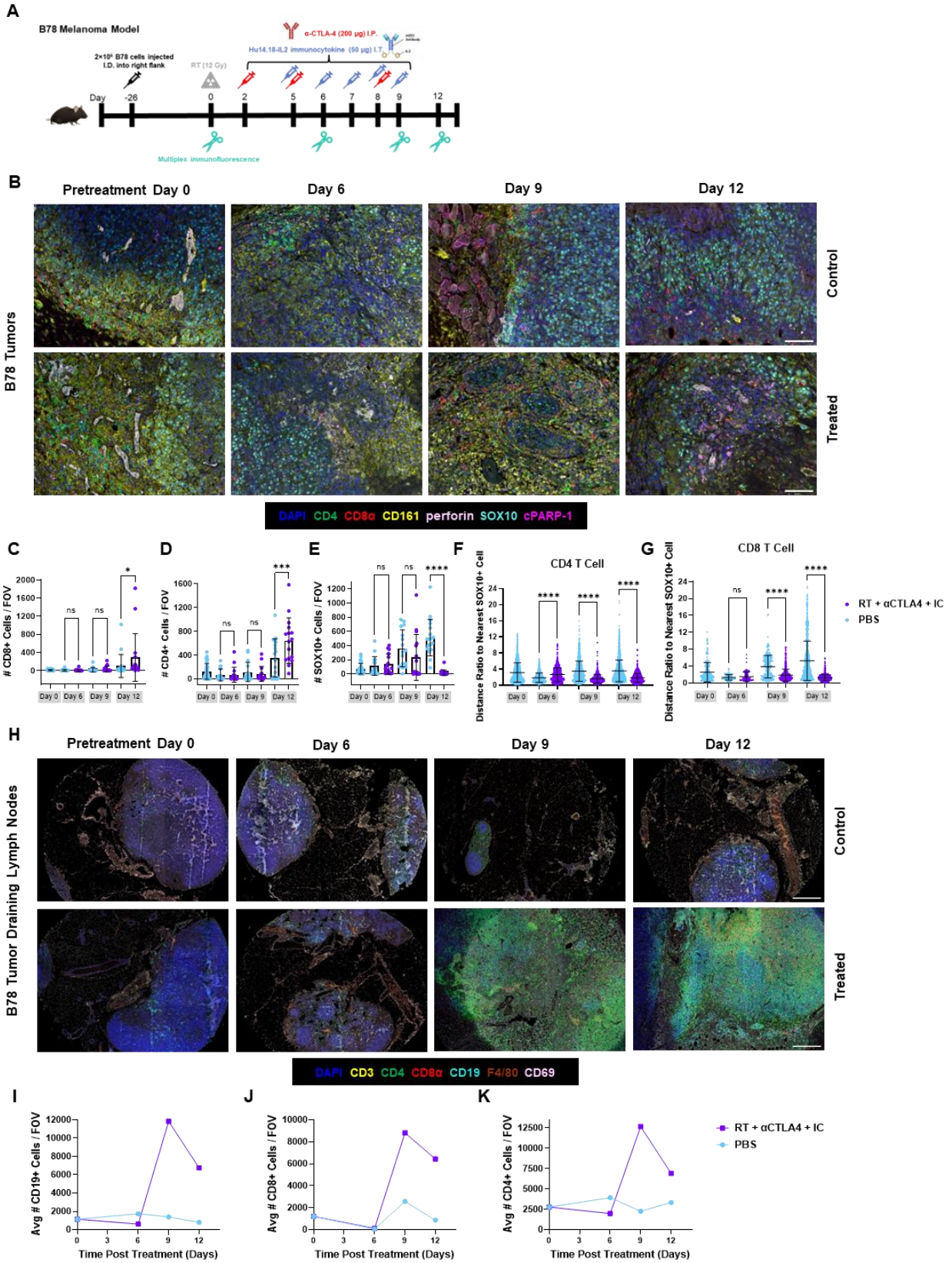
A
B78 Melanoma Model
α-CTLA-4 (200 μg) I.P.
Hu14.18-IL2 immunocytokine (50 μg) I.T.
2×10⁵ B78 cells injected I.D. into right flank
RT (12 Gy)
Day
-26
0
2
5
6
7
8
9
12
Multiplex immunofluorescence
B
Pretreatment Day 0
Day 6
Day 9
Day 12
B78 Tumors
Control
Treated
DAPI CD4 CD8α CD161 perforin SOX10 cPARP-1
C
CD8+ Cells / FOV
D
CD4+ Cells / FOV
E
SOX10+ Cells / FOV
F
CD4 T Cell
Distance Ratio to Nearest SOX10+ Cell
G
CD8 T Cell
RT + αCTLA4 + IC
PBS
ns
****
Day 0
Day 6
Day 9
Day 12
H
Pretreatment Day 0
Day 6
Day 9
Day 12
B78 Tumor Draining Lymph Nodes
Control
Treated
DAPI CD3 CD4 CD8α CD19 F4/80 CD69
I
Avg # CD19+ Cells / FOV
J
Avg # CD8+ Cells / FOV
K
Avg # CD4+ Cells / FOV
Time Post Treatment (Days)
RT + αCTLA4 + IC
PBS

Figure 7. Multiplex immunofluorescence spatial profiling of B78 tumor and lymph node tissues elucidates immune-tumor interactions and infiltration changes with radio-immunotherapy.
A) Experimental timeline where multiplex immunofluorescence was performed on tissues collected during therapy on day 0, 6, 9, and 12. **B)** 20× multiplex immunofluorescence images from B78 tumors across treatment time-course from vehicle (top row) and treated mice (bottom row) (*n* = 2-4 mice per group, 1 experimental replicate, scale bar 100 μm). **C-E)** Quantified CD8+, CD4+, and SOX10+ tumor cells from treated and vehicle B78-bearing mice across treatment time. **F-G)** CD4 and CD8 T cell distance ratio from nearest tumor cell using nearest-neighbor. **H)** Multiplex immunofluorescence images from B78 tumor-draining lymph nodes across treatment time-course from vehicle (top row) and treated mice (bottom row). 3×3 20× images stitched together per lymph node (*n* = 1-2 mice per group, *n* = 9 images per lymph node, 1 experimental replicate, scale bar 300 μm). **I-K)** Quantified CD19+, CD8+, and CD4+ immune cells from lymph nodes from treated and vehicle B78-bearing mice across treatment time (*n* = 1-2 mice per group, *n* = 2-4 lymph nodes per group, 1 experimental replicate, average shown).
C-G) *n* = 2-4 mice per group, *n* = 8 images per tumor, one-way ANOVA, 1 experimental replicate, mean ± SD.

DISCUSSION

Here, we executed a multimodal approach to investigate the therapeutic effects and mechanism of our curative radio-immunotherapy regimen on two contrasting tumor models: immunologically hot MC38 colon carcinoma and immunologically cold B78 melanoma. To facilitate this work, we created an immunocompetent mouse model with CD8 T cells that express mCherry to easily track and monitor CD8 T cell dynamics *in vivo*.

We first examined the immunologically hot MC38 colon carcinoma model. This well-studied tumor model is minimally sensitive to some monotherapies such as glutamine antagonists,[49] and very sensitive to combination therapies such as dual αPD-1 and αCTLA-4 blockade (75% tumor free mice)[78] or dual PD-1 and glutamine antagonist (90% tumor free mice).[49] Here, we showed that MC38 tumors were highly sensitive to our radio-immunotherapy combination with nearly 100% primary and rechallenged tumor rejection. We showed that these tumor responses were primarily driven by a CD8 T cell immune response, as shown by others[73,78,79], though NK and CD4 T cells were also activated and engaged in the immune response. CD8 T cell activation took place early in therapy (Day 6 versus Day 9) based on CD69 expression and increased cell size measured by *in vivo* imaging. As expected, metabolic imaging showed that MC38 CD8 T cells increased glycolysis after priming / activation to fuel their effector function within the tumor (Day 6).[80,81] This is mirrored by increased cytolytic granules and active degranulation shown also on Day 6 via flow cytometry. Later, on Day 9, imaging showed that this immune response was dampened with the CD8 T cells shifting their metabolism back towards an oxidative phenotype, consistent with transition to a memory-like state as others have reported.[49,79,82] We also showed that this oxidative phenotype is not due to exhaustion. These MC38 metabolic dynamics are consistent with other traditional assays such as Seahorse analysis,[49,82] though this is the first time these changes have been shown via *in vivo* label-free metabolic imaging. Interestingly, when we trained a machine learning classifier on MC38 CD8 T or tumor cell *in vivo* metabolic variables, treated versus vehicle mice were accurately classified – showing that our radio-immunotherapy prompts potent immune responses and unique metabolic signatures in both cell types.

Next, we focused on the immunologically cold B78 melanoma model. This GD2+, no MHC-I model is difficult to treat, does not respond to ICI alone, and requires combination therapy for tumor response.[10,17,18,73] We have shown that B78 tumors do respond to the combination of radiation, αCTLA-4, and Hu14.18-IL2 immunocytokine[16,17] with tumor rejections here in 58% of primary tumors and 80% of rechallenged tumors. Interestingly, our immune depletion studies showed that these tumor responses are primarily driven by a CD4 T cell immune response, which has been shown previously,[18,19,83,84] though CD8 and NK cells were also activated and contained cytolytic granules. Changes in tumor infiltrating CD4 cells are minimal, but we observed a large influx of CD4 cells into the tumor draining lymph nodes of treated mice, mirrored by our

work with RT and Hu14.18-IL2 alone[19] – suggesting the key role of CD4 T cells in immune priming, cell signaling, and helper function. A detailed analysis of CD4 function and mechanism within B78 is explored by Erbe *et al,* in work showing that B78 cells do upregulate some MHC-II *in vivo*, but not MHC-I.[19,84] Here we focus on the different roles of CD8 T cells in B78 vs. MC38. Flow cytometry and *in vivo* imaging showed that CD8 T cell activation took place early in therapy for B78 (Day 6), based on CD69 expression and increased cell size. Surprisingly, this CD8 T cell priming / activation was not accompanied by the expected metabolic shift towards glycolysis[85] as seen in MC38; instead the treated CD8 T cells in the B78-bearing mice showed no difference in metabolic profile compared to vehicle . Functionally, the treated CD8 T cells contained increased granzyme B on Days 6 and 12 but there was no evidence of cytolytic activity as CD107a was not expressed on either day, unlike the cytolytic activity for CD8 in MC38. As treatment progressed, these CD8 T cells exhibited an oxidative shift in their metabolism, consistent with a memory or exhausted phenotype, as shown by *in vivo* imaging and scRNAseq. Flow cytometry confirmed increased expression of multiple exhaustion markers on CD8 T cells but not CD4 T cells from B78 treated mice. We expect this lack of effector function, together with the exhaustion and oxidative phenotype is in part due to the minimal to no MHC-I expressed by these B78 melanoma tumors, which recapitulates a common occurrence in the clinical presentation of melanoma.[38,86–89] CD8 T cells are primed and activated early but never receive the full stimulatory signal required to upregulate glycolytic metabolism. Additionally, as little to no MHC-I is present on the tumor cells, these CD8 T cells are not mediating tumor killing, but experience chronic stimulation, likely from cytokines released by the activated CD4 and NK cells, which may eventually lead to exhaustion. Gene expression changes showed that the subsets of CD8 T cells most expanded in treated mice (subsets 5 and 6) upregulated genes related to DNA repair and chromatin activity, mitosis, chemotaxis, and suppression of apoptosis as well as functional changes including increased TCR and IL-17 signaling and NK cell mediated cytotoxicity. Phenotypically, these treated CD8 T cell subsets were diverse with gene expression related to stem-like, cytotoxic, exhausted, and effector memory phenotypes. When we trained a machine learning classifier on B78 CD8 T cell *in vivo* metabolic variables, treated mice versus vehicle mice were consistently classified – showing that our radio-immunotherapy prompts unique metabolic signatures even when CD8 T cells are not driving tumor response. Others have imaged metabolism in immune cells *in vitro* or *in vivo* in a bulk context during immunotherapy[90–92] but, to the best of our knowledge, this is the first time metabolic imaging has been used to monitor changes induced by curative immunotherapy at the single-cell level *in vivo*.

In B78 tumor cells, we observed similar metabolic changes with radio-immunotherapy where treated B78 tumor cells shifted to a more oxidative metabolism over time especially on Days 9 and 12. Gene expression changes of KEGG metabolism pathways showed that tumor cells from treated mice were less metabolically active compared to vehicle mice, consistent with the fact that most of these tumor cells were in the process of dying. Additionally, the remaining tumor cells within treated mice after 8 days of treatment upregulated gene expression related to PD-L1, apoptosis, and increased proliferation / migration. Interestingly, the tumor cells from vehicle mice upregulated gene expression to promote tumor progression including motility, angiogenesis, fibroblast and collagen interactions, and downregulation of apoptosis. Our radio-immunotherapy reduces tumor infiltrating macrophages (involved in collagen production, organization and fibroblast communication) and promotes a healthy collagen phenotype – which may contribute to the change in gene expression observed within the treated mice.[36,93] When focused on gene expression changes related to apoptosis, we observed in the treated mice an increase in genes associated with programmed cell death, NF-κB signaling, and p53 tumor suppressor activity with a decrease in genes associated with cyclic AMP signaling. These gene signatures imply a complex combination of both pro- and anti-apoptotic function within the treated mice.[94–96] Despite these complex mechanisms of cellular attempts towards tumor resistance and escape (PD-L1 increase, migratory phenotype, apoptosis genes), 58% of these mice became tumor free after radio-immunotherapy to the primary tumor. In addition, both CD4 and CD8 T cells from treated mice were in closer proximity to tumor cells compared to vehicle mice, which has been correlated to improved patient survival.[97–100] For the CD4 cells this would be consistent with immune-tumor interaction and immune mediated killing of the MHC-II expressing B78 cells.[84] For the CD8 cells, increased proximity to B78 tumor cells which do not express any detectible MHC-I may be an indicator that

they were in fact closer to antigen presenting cells (APCs) located near tumor cells. Perhaps the APCs processed tumor peptides that could then be presented by APC MHC-I to enable CD8 activation and possibly killing.

Overall, we have shown that curative radio-immunotherapy across hot versus cold tumors produces divergent CD8 T cell metabolic, functional, and genetic phenotypes that correlate to their distinct roles in tumor immunity. Had we only investigated CD8 T cell activation, we would have missed these complex and divergent phenotypes. This work suggests the importance of developing combination therapies that target CD8 T cell exhaustion and also underlines the key role other immune cells (CD4 T, NK) play during tumor response. We believe this is the first time label-free *in vivo* metabolic imaging has been used to study single-cell effects of radio-immunotherapy in preclinical models and correlate the imaging findings at a deep molecular level to flow cytometry, scRNAseq, and multiplex immunofluorescence.

Limitations of the study

We acknowledge there are limitations of murine syngeneic tumor models as the tumors will progress and grow differently than spontaneous tumors. However, this work was important to disentangle the distinct immune responses observed, in response to similar immunotherapy regimens, when applied to our established cold B78 and hot MC38 tumor models. We also acknowledge the limitation of imaging different mice on each time point for our *in vivo* metabolic imaging, as this is a terminal procedure. We considered using a flank imaging window model, to track the same mouse over time, but determined that the window surgery would generate an immune response on its own that would modulate the radio-immunotherapy induced immune response we aimed to study.

RESOURCE AVAILABILITY

Lead contact

Further information and requests for resources and reagents should be directed to and will be fulfilled by the lead contact, Melissa Skala (mcskala@wisc.edu).

Materials availability

CD8-mCherry reporter mice generated in this study will be made available upon request; we may require payment and/or a completed materials transfer agreement.

Data and code availability

- Single-cell RNA-seq data have been deposited at GEO and are publicly available as of the date of publication within Erbe *et al.*[19]
- Original code used to analyze the single-cell RNA-seq data can be found on the GitHub repository reported within Erbe *et al.*[19]
- The raw optical metabolic imaging data supporting the conclusions of this article can be found on GitHub repository.
- Any additional information required to reanalyze the data reported in this paper is available from the lead contact upon request.

ACKNOWLEDGMENTS

This work was supported by a Morgridge Interdisciplinary Postdoctoral Fellowship to A.R.H; The Midwest Athletes against Childhood Cancer Fund; Stand Up to Cancer, The St. Baldrick's Foundation; The Crawdaddy Foundation; The Cancer Research Institute; The Alex's Lemonade Stand Foundation; The End Kids Cancer Foundation; The Hartwell Foundation; The Carol Skornicka Chair in Biomedical Imaging; Retina Research Foundation Daniel M. Albert Chair; and the National Institutes of Health [R35CA197078, 5P30CA014520-40, UL1TR002373, P01CA250972, U54CA232568, R01CA278051, R01CA272855]. The authors would like to acknowledge the University of Wisconsin Small Animal Imaging & Radiotherapy Facility and the University of Wisconsin Carbone Cancer Center Flow Cytometry Laboratory, both supported by P30 CA014520. The authors would like to acknowledge the University of Wisconsin Translational Research Initiatives in Pathology laboratory (TRIP), supported by the UW Department of

Pathology and Laboratory Medicine, UWCCC (P30 CA014520) and the Office of The Director – NIH (S10 OD023526) for assistance, use of their facilities, and creation of a TMA. The TMA was created using a Grand Master Microarrayer (S10 OD023526). The authors would like to thank Sritha Moram for mouse assistance, Wenxuan Zhao for data analysis assistance, Jens Eickhoff and Meredith Hyun for statistical analysis assistance, Matt Stefely for figure formatting assistance, and Alicia Williams for manuscript editing assistance.

AUTHOR CONTRIBUTIONS

Conceptualization, A.R.H., P.M.S., M.C.S., A.K.E., A.L.R.; methodology, A.R.H., A.G., A.H., A.S.F., A.K.E.; Investigation, A.R.H., N.J.B., A.G., A.H., A.S.F., S.K.B., M.A.F, N.W.T., D.V.S., G.M.L., A.A.H., A.D., A.K.E.; writing—original draft, A.R.H.; writing—review & editing, P.M.S. and M.C.S.; funding acquisition, A.R.H., P.M.S., M.C.S.; resources, H.Q.D.; supervision, A.R.H., H.Q.D., P.M.S., M.C.S.

DECLARATION OF INTERESTS

P.M.S. is a volunteer member of the scientific advisory board of Invenra. M.C.S. is a member of the scientific advisory board of Elephas Biosciences Corporation.

DECLARATION OF GENERATIVE AI AND AI-ASSISTED TECHNOLOGIES

During the preparation of this work, no generative AI or AI-assisted technologies were used.

SUPPLEMENTAL INFORMATION

Document S1. Figures S1-S6, Table S1

Figure S1. Characterization of CD8-mCherry reporter mouse shows high specificity of mCherry label to CD8 T cells
A) Construct used to knock-in mCherry near CD8α allele via CRISPR/Cas 9 to create CD8-mCherry reporter mouse model. **B)** CD3+ splenic T cells isolated from wild type C57BL/6J mouse (top) and CD8-mCherry mouse (bottom) and imaged via OMI. All T cells contain NAD(P)H (cyan) while only the reporter mouse expresses mCherry in ~50% of the cells (red) (Scale bar 25 μm). **C)** Multiplex immunofluorescence images of untreated reporter mouse B78 melanoma tumor and spleen show that mCherry is only expressed on cells that co-express CD8 (purple). There is no free mCherry signal (red). There is free CD4 signal (green) as this cell type does not express mCherry (Scale bar 50 μm). **D)** Flow cytometry of untreated B78 melanoma tumors and spleens shows that nearly 100% of CD8 T cells express mCherry while all other immune cells express minimal to no mCherry (n = 10 B78 tumors, n = 8 spleens, mean ± SD, 2 experimental repeats). Characterization across all techniques confirmed the mCherry knock-in was highly specific to CD8α allele providing confidence in subsequent experiments investigating mCherry+ populations.
Figure S2. MC38 and B78 response to radio-immunotherapy repeated in C57BL/6J wild type mice
A) Mean tumor growth curves for treated and vehicle C57BL/6J mice bearing MC38 tumors (pairwise contrasts, n = 5 mice per group, mean ± SEM, 1 representative experiment shown, 3 experimental repeats). **B)** Individual tumor growth curves for treated and vehicle C57BL/6J mice bearing MC38 tumors (n = 5 mice per group, 1 representative experiment shown, 3 experimental repeats). **C)** Kaplan-Meier survival curve showing % survival of treated and vehicle C57BL/6J mice bearing MC38 tumors (pairwise log-rank test, n = 46 mice, 3 experimental repeats combined). **D)** Number of tumor free C57BL/6J mice from treated and vehicle primary MC38 tumors (Fisher exact test, n = 46, 3 experimental repeats) and mice from treated and naïve MC38 tumor rechallenge 2 months later (Fisher exact test, n = 32, 3 experimental repeats). **E)** Mean tumor growth curves for treated and vehicle C57BL/6J mice bearing B78 tumors (pairwise contrasts, n = 5 mice per group, mean ± SEM, 1 representative experiment shown, 3 experimental repeats). **F)** Individual tumor growth curves for treated and vehicle C57BL/6J mice bearing B78 tumors (n = 5 mice per group, 1 representative experiment shown, 3 experimental repeats). **G)** Kaplan-Meier survival curve showing % survival of treated and vehicle C57BL/6J mice bearing B78 tumors (pairwise log-rank test, n = 36 mice, 3 experimental repeats combined). **H)** Number of tumor free C57BL/6J mice from treated and vehicle primary B78 tumors (Fisher exact test, n = 36, 3 experimental repeats) and mice from treated and naïve B78 tumor rechallenge 2 months later (Fisher exact test, n = 30, 3 experimental repeats) (*p < 0.05, **p < 0.01, ***p < 0.001, ****p < 0.0001).

Figure S3. Flow cytometry gating strategies with additional MC38 and B78 flow data
A) Flow cytometry gating phenotype used for all immune cell populations in Figures 1,3, and S3. **B)** Flow cytometry of NKT, B, macrophages, neutrophils, and DCs from treated and vehicle MC38 tumor bearing mice across treatment time (one-way ANOVA, n = 5-20 mice per group, 2-4 experimental repeats, mean ± SD, % CD45+ cells). **C-E)** Flow cytometry of CD4 activation, effector function, and exhaustion from treated and vehicle MC38 tumor bearing mice across treatment time. **F)** Flow cytometry NKT, B, macrophages, and neutrophils from treated and vehicle B78 tumor bearing mice across treatment time (one-way ANOVA, n = 10 mice per group, 2 experimental repeats, mean ± SD, % CD45+ cells). **G-I)** Flow cytometry of NK cell activation, effector function, and exhaustion from treated and vehicle B78 tumor bearing mice across treatment time (*p < 0.05, **p < 0.01, ***p < 0.001, ****p < 0.0001).
C-E) n = 10-20 mice per group, one-way ANOVA, mean ± SD, % CD4+ cells, 2-4 experimental repeats.
G-I) n = 10-20 mice per group, one-way ANOVA, mean ± SD, % NK+ cells, 2-4 experimental repeats.
Figure S4. Optical metabolic imaging of *in vitro* MC38 metabolic changes with electron transport chain (NaCN) and glycolysis (2DG) metabolic inhibitor treatments
A-K) Quantified single cell MC38 metabolic changes with NaCN treatment (n = 932 pre-treatment cells, n = 1154 post-treatment NaCN cells). **See Table S1** for parameter definitions. **L-V)** Quantified single cell MC38 metabolic changes with 2DG treatment (n = 643 pre-treatment cells, n = 612 post-treatment 2DG cells) (*p < 0.05, **p < 0.01, ***p < 0.001, ****p < 0.0001). See **Table S1** for parameter definitions.
A-V) 2 technical replicates, 2 experimental repeats, unpaired T test *p < 0.05, ****p < 0.0001, Glass's Δ, mean ±SD.
Figure S5. Optical metabolic imaging of *in vitro* B78 metabolic changes with electron transport chain (NaCN) and glycolysis (2DG) metabolic inhibitor treatments
A-K) Quantified single cell B78 metabolic changes with NaCN treatment (n = 1488 pre-treatment cells, n = 1393 post-treatment NaCN cells). **L-V)** Quantified single cell B78 metabolic changes with 2DG treatment (n = 1113 pre-treatment cells, n = 1589 post-treatment 2DG cells) (*p < 0.05, **p < 0.01, ***p < 0.001, ****p < 0.0001).
A-V) 2 technical replicates, 2 experimental repeats, unpaired T test, **p < 0.01, ****p < 0.0001, Glass's Δ, mean ± SD.
Figure S6. Single channel B78 tumor and lymph node immunofluorescence images with additional quantified data
A) 20× single channel B78 tumor immunofluorescence images at day 0 and 12 of treatment (n = 2-4 mice per group, 1 experimental replicate, scale bar 100 μm). **B-C)** Quantified changes within B78 tumor images of perforin and cPARP-1 (n = 2-4 mice per group, n = 8 images per tumor, 1 experimental replicate, one-way ANOVA, mean ± SD). **D)** Quantified CD69+ cells from lymph nodes from treated and vehicle B78 tumor bearing mice at day 0 and 12 of treatment (n = 1-2 mice per group, n = 2-4 lymph node per group, 1 experimental replicate, average shown). **E)** Single channel immunofluorescence images from B78 tumor-draining lymph nodes at day 0 and 12 of treatment. 3×3 20× images stitched together per lymph node (n = 1-2 mice per group, n = 9 images per lymph node, 1 experimental replicate, scale bar 300 μm) (*p < 0.05, **p < 0.01, ***p < 0.001, ****p < 0.0001).
Table S1. Fluorescence lifetime imaging and morphology parameters.

REFERENCES

1. Emens, L.A., Romero, P.J., Anderson, A.C., Bruno, T.C., Capitini, C.M., Collyar, D., Gulley, J.L., Hwu, P., Posey, A.D., Silk, A.W., et al. (2024). Challenges and opportunities in cancer immunotherapy: a Society for Immunotherapy of Cancer (SITC) strategic vision. J Immunother Cancer *12*, e009063. https://doi.org/10.1136/jitc-2024-009063.

2. Kruger, S., Ilmer, M., Kobold, S., Cadilha, B.L., Endres, S., Ormanns, S., Schuebbe, G., Renz, B.W., D'Haese, J.G., Schloesser, H., et al. (2019). Advances in cancer immunotherapy 2019 – latest trends. J Exp Clin Cancer Res *38*, 268. https://doi.org/10.1186/s13046-019-1266-0.

3. Pointer, K.B., Pitroda, S.P., and Weichselbaum, R.R. (2022). Radiotherapy and immunotherapy: open questions and future strategies. Trends in Cancer *8*, 9–20. https://doi.org/10.1016/j.trecan.2021.10.003.

4. Rakhmilevich, A.L., Baldeshwiler, M.J., Van De Voort, T.J., Felder, M.A.R., Yang, R.K., Kalogriopoulos, N.A., Koslov, D.S., Van Rooijen, N., and Sondel, P.M. (2012). Tumor-associated myeloid cells can be activated in vitro and in vivo to mediate antitumor effects. Cancer Immunol Immunother *61*, 1683–1697. https://doi.org/10.1007/s00262-012-1236-2.

5. Voeller, J., Erbe, A.K., Slowinski, J., Rasmussen, K., Carlson, P.M., Hoefges, A., VandenHeuvel, S., Stuckwisch, A., Wang, X., Gillies, S.D., et al. (2019). Combined innate and adaptive immunotherapy overcomes resistance of immunologically cold syngeneic murine neuroblastoma to checkpoint inhibition. J. Immunother. Cancer *7*, 344. https://doi.org/10.1186/s40425-019-0823-6.

6. Aiken, T.J., Erbe, A.K., Zebertavage, L., Komjathy, D., Feils, A.S., Rodriguez, M., Stuckwisch, A., Gillies, S.D., Morris, Z.S., Birstler, J., et al. (2022). Mechanism of effective combination radio-immunotherapy against 9464D-GD2, an immunologically cold murine neuroblastoma. J. Immunother. Cancer *10*, e004834. https://doi.org/10.1136/jitc-2022-004834.

7. Zebertavage, L., Schopf, A., Nielsen, M., Matthews, J., Erbe, A.K., Aiken, T.J., Katz, S., Sun, C., Witt, C.M., Rakhmilevich, A.L., et al. (2024). Evaluation of a Combinatorial Immunotherapy Regimen That Can Cure Mice Bearing MYCN-Driven High-Risk Neuroblastoma That Resists Current Clinical Therapy. JCM *13*, 2561. https://doi.org/10.3390/jcm13092561.

8. Rakhmilevich, A.L., Tsarovsky, N.W., Felder, M., Zaborek, J., Moram, S., Erbe, A.K., Pieper, A.A., Spiegelman, D.V., Cheng, E.M., Witt, C.M., et al. (2024). A combined radio-immunotherapy regimen eradicates late-stage tumors in mice. Front Immunol *15*, 1419773. https://doi.org/10.3389/fimmu.2024.1419773.

9. Carlson, P.M., Patel, R.B., Birstler, J., Rodriquez, M., Sun, C., Erbe, A.K., Bates, A.M., Marsh, I., Grudzinski, J., Hernandez, R., et al. (2023). Radiation to all macroscopic sites of tumor permits greater systemic antitumor response to in situ vaccination. J Immunother Cancer *11*, e005463. https://doi.org/10.1136/jitc-2022-005463.

10. Pieper, A.A., Rakhmilevich, A.L., Spiegelman, D.V., Patel, R.B., Birstler, J., Jin, W.J., Carlson, P.M., Charych, D.H., Hank, J.A., Erbe, A.K., et al. (2021). Combination of radiation therapy, bempegaldesleukin, and checkpoint blockade eradicates advanced solid tumors and metastases in mice. J Immunother Cancer *9*, e002715. https://doi.org/10.1136/jitc-2021-002715.

11. Pieper, A.A., Zangl, L.M., Speigelman, D.V., Feils, A.S., Hoefges, A., Jagodinsky, J.C., Felder, M.A., Tsarovsky, N.W., Arthur, I.S., Brown, R.J., et al. (2021). Radiation Augments the Local Anti-Tumor Effect of In Situ Vaccine With CpG-Oligodeoxynucleotides and Anti-OX40 in Immunologically Cold Tumor Models. Front Immunol *12*, 763888. https://doi.org/10.3389/fimmu.2021.763888.

12. Upadhaya, S., Neftelinov, S.T., Hodge, J., and Campbell, J. (2022). Challenges and opportunities in the PD1/PDL1 inhibitor clinical trial landscape. Nature Reviews Drug Discovery *21*, 482–483. https://doi.org/10.1038/d41573-022-00030-4.

13. Larkin, J., Chiarion-Sileni, V., Gonzalez, R., Grob, J.-J., Rutkowski, P., Lao, C.D., Cowey, C.L., Schadendorf, D., Wagstaff, J., Dummer, R., et al. (2019). Five-Year Survival with Combined Nivolumab and Ipilimumab in Advanced Melanoma. New England Journal of Medicine *381*, 1535–1546. https://doi.org/10.1056/NEJMoa1910836.

14. Wolchok, J.D., Chiarion-Sileni, V., Gonzalez, R., Grob, J.-J., Rutkowski, P., Lao, C.D., Cowey, C.L., Schadendorf, D., Wagstaff, J., Dummer, R., et al. (2021). Long-Term Outcomes With Nivolumab Plus Ipilimumab or Nivolumab Alone Versus Ipilimumab in Patients With Advanced Melanoma. Journal of Clinical Oncology. https://doi.org/10.1200/JCO.21.02229.

15. Zaidi, N., and Jaffee, E.M. Immunotherapy transforms cancer treatment. J Clin Invest *129*, 46–47. https://doi.org/10.1172/JCI126046.

16. Morris, Z.S., Guy, E.I., Francis, D.M., Gressett, M.M., Werner, L.R., Carmichael, L.L., Yang, R.K., Armstrong, E.A., Huang, S., Navid, F., et al. (2016). *In Situ* Tumor Vaccination by Combining Local Radiation and Tumor-Specific Antibody or Immunocytokine Treatments. Cancer Research *76*, 3929–3941. https://doi.org/10.1158/0008-5472.CAN-15-2644.

17. Morris, Z.S., Guy, E.I., Werner, L.R., Carlson, P.M., Heinze, C.M., Kler, J.S., Busche, S.M., Jaquish, A.A., Sriramaneni, R.N., Carmichael, L.L., et al. (2018). Tumor-Specific Inhibition of *In Situ* Vaccination by Distant Untreated Tumor Sites. Cancer Immunology Research *6*, 825–834. https://doi.org/10.1158/2326-6066.CIR-17-0353.

18. Aiken, T.J., Komjathy, D., Rodriguez, M., Stuckwisch, A., Feils, A., Subbotin, V., Birstler, J., Gillies, S.D., Rakhmilevich, A.L., Erbe, A.K., et al. (2022). Short-course neoadjuvant in situ vaccination for murine melanoma. J Immunother Cancer *10*, e003586. https://doi.org/10.1136/jitc-2021-003586.

19. Erbe, A.K., Feils, A.S., Gao, A., VandenHeuvel, S., Boyenga, S., Hampton, A.A., Heck, M., Slowinski, J., Spiegelman, D.V., Tsarovsky, N.W., et al. (2025). CD4 T cell driven anti-tumor response in MHCII+ melanoma. Preprint at bioRxiv.

20. Saez-Ibanez, A.R., Upadhaya, S., and Campbell, J. (2023). Immuno-oncology clinical trials take a turn beyond PD1/PDL1 inhibitors. Nature Reviews Drug Discovery *22*, 442–443. https://doi.org/10.1038/d41573-023-00066-0.

21. Raskov, H., Orhan, A., Christensen, J.P., and Gögenur, I. (2021). Cytotoxic CD8+ T cells in cancer and cancer immunotherapy. Br J Cancer *124*, 359–367. https://doi.org/10.1038/s41416-020-01048-4.

22. Waldman, A.D., Fritz, J.M., and Lenardo, M.J. (2020). A guide to cancer immunotherapy: from T cell basic science to clinical practice. Nat Rev Immunol *20*, 651–668. https://doi.org/10.1038/s41577-020-0306-5.

23. Zhang, N., and Bevan, M.J. (2011). CD8+ T Cells: Foot Soldiers of the Immune System. Immunity *35*, 161–168. https://doi.org/10.1016/j.immuni.2011.07.010.

24. Baker, A.T., Abuwarwar, M.H., Poly, L., Wilkins, S., and Fletcher, A.L. (2021). Cancer-Associated Fibroblasts and T Cells: From Mechanisms to Outcomes. The Journal of Immunology *206*, 310–320. https://doi.org/10.4049/jimmunol.2001203.

25. Henke, E., Nandigama, R., and Ergün, S. (2020). Extracellular Matrix in the Tumor Microenvironment and Its Impact on Cancer Therapy. Frontiers in Molecular Biosciences *6*.

26. Melero, I., Rouzaut, A., Motz, GregT., and Coukos, G. (2014). T-Cell and NK-Cell Infiltration into Solid Tumors: A Key Limiting Factor for Efficacious Cancer Immunotherapy. Cancer Discov *4*, 522–526. https://doi.org/10.1158/2159-8290.CD-13-0985.

27. Schaer, D.A., Lesokhin, A.M., and Wolchok, J.D. (2011). Hiding the road signs that lead to tumor immunity. J Exp Med *208*, 1937–1940. https://doi.org/10.1084/jem.20111856.

28. Augustin, R.C., Delgoffe, G.M., and Najjar, Y.G. (2020). Characteristics of the Tumor Microenvironment That Influence Immune Cell Functions: Hypoxia, Oxidative Stress, Metabolic Alterations. Cancers (Basel) *12*, 3802. https://doi.org/10.3390/cancers12123802.

29. DePeaux, K., Rivadeneira, D.B., Lontos, K., Dean, V.G., Gunn, W.G., Watson, M.J., Yao, T., Wilfahrt, D., Hinck, C., Wieteska, L., et al. (2023). An oncolytic virus-delivered TGFβ inhibitor overcomes the immunosuppressive tumor microenvironment. J Exp Med *220*, e20230053. https://doi.org/10.1084/jem.20230053.

30. Watson, M.J., and Delgoffe, G.M. (2022). Fighting in a wasteland: deleterious metabolites and antitumor immunity. J Clin Invest *132*, e148549. https://doi.org/10.1172/JCI148549.

31. Scharping, N.E., Menk, A.V., Moreci, R.S., Whetstone, R.D., Dadey, R.E., Watkins, S.C., Ferris, R.L., and Delgoffe, G.M. (2016). The Tumor Microenvironment Represses T Cell Mitochondrial Biogenesis to Drive Intratumoral T Cell Metabolic Insufficiency and Dysfunction. Immunity *45*, 374–388. https://doi.org/10.1016/j.immuni.2016.07.009.

32. Yang, M., Du, W., Yi, L., Wu, S., He, C., Zhai, W., Yue, C., Sun, R., Menk, A.V., Delgoffe, G.M., et al. (2020). Checkpoint molecules coordinately restrain hyperactivated effector T cells in the tumor microenvironment. Oncoimmunology *9*, 1708064. https://doi.org/10.1080/2162402X.2019.1708064.

33. Sahai, E., Astsaturov, I., Cukierman, E., DeNardo, D.G., Egeblad, M., Evans, R.M., Fearon, D., Greten, F.R., Hingorani, S.R., Hunter, T., et al. (2020). A framework for advancing our understanding of cancer-associated fibroblasts. Nat Rev Cancer *20*, 174–186. https://doi.org/10.1038/s41568-019-0238-1.

34. Piersma, B., Hayward, M.-K., and Weaver, V.M. (2020). Fibrosis and cancer: A strained relationship. Biochim Biophys Acta Rev Cancer *1873*, 188356. https://doi.org/10.1016/j.bbcan.2020.188356.

35. Tharp, K.M., Kersten, K., Maller, O., Timblin, G.A., Stashko, C., Canale, F.P., Menjivar, R.E., Hayward, M.-K., Berestjuk, I., Ten Hoeve, J., et al. (2024). Tumor-associated macrophages restrict CD8+ T cell function through collagen deposition and metabolic reprogramming of the breast cancer microenvironment. Nat Cancer *5*, 1045–1062. https://doi.org/10.1038/s43018-024-00775-4.

36. Maller, O., Drain, A.P., Barrett, A.S., Borgquist, S., Ruffell, B., Zakharevich, I., Pham, T.T., Gruosso, T., Kuasne, H., Lakins, J.N., et al. (2021). Tumour-associated macrophages drive stromal cell-dependent collagen crosslinking and stiffening to promote breast cancer aggression. Nat Mater *20*, 548–559. https://doi.org/10.1038/s41563-020-00849-5.

37. Taylor, B.C., and Balko, J.M. (2022). Mechanisms of MHC-I Downregulation and Role in Immunotherapy Response. Front Immunol *13*, 844866. https://doi.org/10.3389/fimmu.2022.844866.

38. Mengoni, M., Mahlo, F.O., Gaffal, E., Tüting, T., and Braun, A.D. (2025). Downregulation of MHC-I on Melanoma Cells and Decreased CD8+ T-Cell Infiltration Are Associated With Metastatic Spread

and Resistance to Immunotherapy. Lab Invest *105*, 102209. https://doi.org/10.1016/j.labinv.2024.102209.

39. Apostolova, P., and Pearce, E.L. (2022). Lactic acid and lactate: revisiting the physiological roles in the tumor microenvironment. Trends Immunol *43*, 969–977. https://doi.org/10.1016/j.it.2022.10.005.

40. Molgora, M., Esaulova, E., Vermi, W., Hou, J., Chen, Y., Luo, J., Brioschi, S., Bugatti, M., Omodei, A.S., Ricci, B., et al. (2020). TREM2 Modulation Remodels the Tumor Myeloid Landscape Enhancing Anti-PD-1 Immunotherapy. Cell *182*, 886-900.e17. https://doi.org/10.1016/j.cell.2020.07.013.

41. Renner, K., Singer, K., Koehl, G.E., Geissler, E.K., Peter, K., Siska, P.J., and Kreutz, M. (2017). Metabolic Hallmarks of Tumor and Immune Cells in the Tumor Microenvironment. Front. Immunol. *8*. https://doi.org/10.3389/fimmu.2017.00248.

42. Roy, D.G., Kaymak, I., Williams, K.S., Ma, E.H., and Jones, R.G. (2021). Immunometabolism in the Tumor Microenvironment. Annual Review of Cancer Biology *5*, 137–159. https://doi.org/10.1146/annurev-cancerbio-030518-055817.

43. Hanahan, D. (2022). Hallmarks of Cancer: New Dimensions. Cancer Discovery *12*, 31–46. https://doi.org/10.1158/2159-8290.CD-21-1059.

44. DePeaux, K., and Delgoffe, G.M. (2021). Metabolic barriers to cancer immunotherapy. Nat Rev Immunol *21*, 785–797. https://doi.org/10.1038/s41577-021-00541-y.

45. Park, J., Hsueh, P.-C., Li, Z., and Ho, P.-C. (2023). Microenvironment-driven metabolic adaptations guiding CD8+ T cell anti-tumor immunity. Immunity *56*, 32–42. https://doi.org/10.1016/j.immuni.2022.12.008.

46. Chang, C.-H., Qiu, J., O'Sullivan, D., Buck, M.D., Noguchi, T., Curtis, J.D., Chen, Q., Gindin, M., Gubin, M.M., van der Windt, G.J.W., et al. (2015). Metabolic Competition in the Tumor Microenvironment Is a Driver of Cancer Progression. Cell *162*, 1229–1241. https://doi.org/10.1016/j.cell.2015.08.016.

47. Vignali, P.D.A., DePeaux, K., Watson, M.J., Ye, C., Ford, B.R., Lontos, K., McGaa, N.K., Scharping, N.E., Menk, A.V., Robson, S.C., et al. (2023). Hypoxia drives CD39-dependent suppressor function in exhausted T cells to limit antitumor immunity. Nat Immunol *24*, 267–279. https://doi.org/10.1038/s41590-022-01379-9.

48. Leone, R.D., and Powell, J.D. (2020). Metabolism of immune cells in cancer. Nat Rev Cancer *20*, 516–531. https://doi.org/10.1038/s41568-020-0273-y.

49. Leone, R.D., Zhao, L., Englert, J.M., Sun, I.-M., Oh, M.-H., Sun, I.-H., Arwood, M.L., Bettencourt, I.A., Patel, C.H., Wen, J., et al. (2019). Glutamine blockade induces divergent metabolic programs to overcome tumor immune evasion. Science *366*, 1013–1021. https://doi.org/10.1126/science.aav2588.

50. Delgoffe, G.M., and Powell, J.D. (2015). Feeding an army: The metabolism of T cells in activation, anergy, and exhaustion. Mol Immunol *68*, 492–496. https://doi.org/10.1016/j.molimm.2015.07.026.

51. Ghesquière, B., Wong, B.W., Kuchnio, A., and Carmeliet, P. (2014). Metabolism of stromal and immune cells in health and disease. Nature *511*, 167–176. https://doi.org/10.1038/nature13312.

52. Klein Geltink, R.I., Kyle, R.L., and Pearce, E.L. (2018). Unraveling the Complex Interplay Between T Cell Metabolism and Function. Annu. Rev. Immunol. *36*, 461–488. https://doi.org/10.1146/annurev-immunol-042617-053019.

53. Mockler, M.B., Conroy, M.J., and Lysaght, J. (2014). Targeting T cell immunometabolism for cancer immunotherapy; understanding the impact of the tumor microenvironment. Front Oncol *4*, 107. https://doi.org/10.3389/fonc.2014.00107.

54. Kishton, R.J., Sukumar, M., and Restifo, N.P. (2017). Metabolic Regulation of T Cell Longevity and Function in Tumor Immunotherapy. Cell Metabolism *26*, 94–109. https://doi.org/10.1016/j.cmet.2017.06.016.

55. O'Sullivan, D., Sanin, D.E., Pearce, E.J., and Pearce, E.L. (2019). Metabolic interventions in the immune response to cancer. Nat Rev Immunol *19*, 324–335. https://doi.org/10.1038/s41577-019-0140-9.

56. Pearce, E.L. (2021). Metabolism as a driver of immunity. Nat Rev Immunol *21*, 618–619. https://doi.org/10.1038/s41577-021-00601-3.

57. Corrado, M., and Pearce, E.L. (2022). Targeting memory T cell metabolism to improve immunity. J Clin Invest *132*, e148546. https://doi.org/10.1172/JCI148546.

58. Pearce, E.L., and Pearce, E.J. (2013). Metabolic pathways in immune cell activation and quiescence. Immunity *38*, 633–643. https://doi.org/10.1016/j.immuni.2013.04.005.

59. Chance, B., Schoener, B., Oshino, R., Itshak, F., and Nakase, Y. (1979). Oxidation-reduction ratio studies of mitochondria in freeze-trapped samples. NADH and flavoprotein fluorescence signals. Journal of Biological Chemistry *254*, 4764–4771. https://doi.org/10.1016/S0021-9258(17)30079-0.

60. Georgakoudi, I., and Quinn, K.P. (2012). Optical Imaging Using Endogenous Contrast to Assess Metabolic State. Annu. Rev. Biomed. Eng. *14*, 351–367. https://doi.org/10.1146/annurev-bioeng-071811-150108.

61. Hull, R.V., Conger, P.S., and Hoobler, R.J. (2001). Conformation of NADH studied by fluorescence excitation transfer spectroscopy. Biophysical Chemistry *90*, 9–16. https://doi.org/10.1016/S0301-4622(00)00239-8.

62. Lakowicz, J.R. (1992). Fluorescence lifetime imaging of free and protein-bound NADH. Proc. Natl. Acad. Sci. *89*, 1271–1275.

63. Datta, R., Heaster, T.M., Sharick, J.T., Gillette, A.A., and Skala, M.C. (2020). Fluorescence lifetime imaging microscopy: fundamentals and advances in instrumentation, analysis, and applications. J. Biomed. Opt. *25*, 1. https://doi.org/10.1117/1.JBO.25.7.071203.

64. Blacker, T.S., Mann, Z.F., Gale, J.E., Ziegler, M., Bain, A.J., Szabadkai, G., and Duchen, M.R. (2014). Separating NADH and NADPH fluorescence in live cells and tissues using FLIM. Nat Commun *5*, 3936. https://doi.org/10.1038/ncomms4936.

65. Skala, M.C., Riching, K.M., Gendron-Fitzpatrick, A., Eickhoff, J., Eliceiri, K.W., White, J.G., and Ramanujam, N. (2007). *In vivo* multiphoton microscopy of NADH and FAD redox states, fluorescence lifetimes, and cellular morphology in precancerous epithelia. Proc. Natl. Acad. Sci. U.S.A. *104*, 19494–19499. https://doi.org/10.1073/pnas.0708425104.

66. Heaton, A.R., Rehani, P.R., Hoefges, A., Lopez, A.F., Erbe, A.K., Sondel, P.M., and Skala, M.C. (2023). Single cell metabolic imaging of tumor and immune cells in vivo in melanoma bearing mice. Front. Oncol. *13*, 1110503. https://doi.org/10.3389/fonc.2023.1110503.

67. Walsh, A.J., Mueller, K.P., Tweed, K., Jones, I., Walsh, C.M., Piscopo, N.J., Niemi, N.M., Pagliarini, D.J., Saha, K., and Skala, M.C. (2020). Classification of T-cell activation via autofluorescence lifetime imaging. Nat Biomed Eng *5*, 77–88. https://doi.org/10.1038/s41551-020-0592-z.

68. Heaster, T.M., Heaton, A.R., Sondel, P.M., and Skala, M.C. (2021). Intravital Metabolic Autofluorescence Imaging Captures Macrophage Heterogeneity Across Normal and Cancerous Tissue. Front. Bioeng. Biotechnol. *9*, 644648. https://doi.org/10.3389/fbioe.2021.644648.

69. Miskolci, V., Tweed, K.E., Lasarev, M.R., Britt, E.C., Walsh, A.J., Zimmerman, L.J., McDougal, C.E., Cronan, M.R., Fan, J., Sauer, J.-D., et al. (2022). In vivo fluorescence lifetime imaging of macrophage intracellular metabolism during wound responses in zebrafish. eLife *11*, e66080. https://doi.org/10.7554/eLife.66080.

70. Pham, D.L., Cappabianca, D., Forsberg, M.H., Weaver, C., Mueller, K.P., Tommasi, A., Vidugiriene, J., Lauer, A., Sylvester, K., Bugel, M., et al. (2024). Label free metabolic imaging to enhance the efficacy of Chimeric Antigen Receptor T cell therapy. BioRxiv.

71. Cappabianca, D., Pham, D., Forsberg, M.H., Bugel, M., Tommasi, A., Lauer, A., Vidugiriene, J., Hrdlicka, B., McHale, A., Sodji, Q.H., et al. (2024). Metabolic priming of GD2 TRAC-CAR T cells during manufacturing promotes memory phenotypes while enhancing persistence. Mol Ther Methods Clin Dev *32*, 101249. https://doi.org/10.1016/j.omtm.2024.101249.

72. Fabian, K.P., Padget, M.R., Fujii, R., Schlom, J., and Hodge, J.W. (2021). Differential combination immunotherapy requirements for inflamed (warm) tumors versus T cell excluded (cool) tumors: engage, expand, enable, and evolve. J Immunother Cancer *9*. https://doi.org/10.1136/jitc-2020-001691.

73. Ray, A., Bassette, M., Hu, K.H., Pass, L.F., Courau, T., Samad, B., Combes, A.J., Johri, V., Davidson, B., Wai, K., et al. (2025). Multimodal delineation of a layer of effector function among exhausted CD8 T cells in tumors. Science Immunology *10*, eadt3537. https://doi.org/10.1126/sciimmunol.adt3537.

74. Carlson, P.M., Mohan, M., Rodriguez, M., Subbotin, V., Sun, C.X., Patel, R.B., Birstler, J., Hank, J.A., Rakhmilevich, A.L., Morris, Z.S., et al. (2021). Depth of tumor implantation affects response to in situ vaccination in a syngeneic murine melanoma model. J Immunother Cancer *9*, e002107. https://doi.org/10.1136/jitc-2020-002107.

75. Kanehisa, M. (2019). Toward understanding the origin and evolution of cellular organisms. Protein Science *28*, 1947–1951. https://doi.org/10.1002/pro.3715.

76. Kanehisa, M., and Goto, S. (2000). KEGG: Kyoto Encyclopedia of Genes and Genomes. Nucleic Acids Research *28*, 27–30. https://doi.org/10.1093/nar/28.1.27.

77. Kanehisa, M., Furumichi, M., Sato, Y., Matsuura, Y., and Ishiguro-Watanabe, M. (2025). KEGG: biological systems database as a model of the real world. Nucleic Acids Research *53*, D672–D677. https://doi.org/10.1093/nar/gkae909.

78. Selby, M.J., Engelhardt, J.J., Johnston, R.J., Lu, L.-S., Han, M., Thudium, K., Yao, D., Quigley, M., Valle, J., Wang, C., et al. (2016). Preclinical Development of Ipilimumab and Nivolumab Combination Immunotherapy: Mouse Tumor Models, In Vitro Functional Studies, and Cynomolgus Macaque Toxicology. PLoS ONE *11*, e0161779. https://doi.org/10.1371/journal.pone.0161779.

79. Lee, K.L., Benz, S.C., Hicks, K.C., Nguyen, A., Gameiro, S.R., Palena, C., Sanborn, J.Z., Su, Z., Ordentlich, P., Rohlin, L., et al. (2019). Efficient Tumor Clearance and Diversified Immunity through Neoepitope Vaccines and Combinatorial Immunotherapy. Cancer Immunol Res *7*, 1359–1370. https://doi.org/10.1158/2326-6066.CIR-18-0620.

80. Pearce, E.L., Poffenberger, M.C., Chang, C.-H., and Jones, R.G. (2013). Fueling Immunity: Insights into Metabolism and Lymphocyte Function. Science *342*, 1242454. https://doi.org/10.1126/science.1242454.

81. Siska, P.J., Beckermann, K.E., Mason, F.M., Andrejeva, G., Greenplate, A.R., Sendor, A.B., Chiang, Y.-C.J., Corona, A.L., Gemta, L.F., Vincent, B.G., et al. (2017). Mitochondrial dysregulation and glycolytic insufficiency functionally impair CD8 T cells infiltrating human renal cell carcinoma. JCI Insight *2*. https://doi.org/10.1172/jci.insight.93411.

82. van der Windt, G.J.W., Everts, B., Chang, C.-H., Curtis, J.D., Freitas, T.C., Amiel, E., Pearce, E.J., and Pearce, E.L. (2012). Mitochondrial Respiratory Capacity Is a Critical Regulator of CD8+ T Cell Memory Development. Immunity *36*, 68–78. https://doi.org/10.1016/j.immuni.2011.12.007.

83. Bawden, E.G., Wagner, T., Schröder, J., Effern, M., Hinze, D., Newland, L., Attrill, G.H., Lee, A.R., Engel, S., Freestone, D., et al. (2024). CD4+ T cell immunity against cutaneous melanoma encompasses multifaceted MHC II–dependent responses. Science Immunology *9*, eadi9517. https://doi.org/10.1126/sciimmunol.adi9517.

84. Erbe, A.K., Feils, A.S., Hampton, A., Spiegelman, D., Tsarovsky, N., Hoefges, A., Carlson, P.M., Pieper, A., Haertle, C., Heck, M., et al. (2023). Abstract 4142: CD4 T cell-driven response to immunotherapy against mouse melanoma tumors. Cancer Research *83*, 4142. https://doi.org/10.1158/1538-7445.AM2023-4142.

85. Menk, A.V., Scharping, N.E., Moreci, R.S., Zeng, X., Guy, C., Salvatore, S., Bae, H., Xie, J., Young, H.A., Wendell, S.G., et al. (2018). Early TCR Signaling Induces Rapid Aerobic Glycolysis Enabling Distinct Acute T Cell Effector Functions. Cell Rep *22*, 1509–1521. https://doi.org/10.1016/j.celrep.2018.01.040.

86. Dhatchinamoorthy, K., Colbert, J.D., and Rock, K.L. (2021). Cancer Immune Evasion Through Loss of MHC Class I Antigen Presentation. Front. Immunol. *12*. https://doi.org/10.3389/fimmu.2021.636568.

87. Hicklin, D.J., Wang, Z., Arienti, F., Rivoltini, L., Parmiani, G., and Ferrone, S. (1998). beta2-Microglobulin mutations, HLA class I antigen loss, and tumor progression in melanoma. J Clin Invest *101*, 2720–2729. https://doi.org/10.1172/JCI498.

88. Restifo, N.P., Marincola, F.M., Kawakami, Y., Taubenberger, J., Yannelli, J.R., and Rosenberg, S.A. (1996). Loss of Functional Beta 2 -Microglobulin in Metastatic Melanomas From Five Patients Receiving Immunotherapy. JNCI: Journal of the National Cancer Institute *88*, 100–108. https://doi.org/10.1093/jnci/88.2.100.

89. Lee, J.H., Shklovskaya, E., Lim, S.Y., Carlino, M.S., Menzies, A.M., Stewart, A., Pedersen, B., Irvine, M., Alavi, S., Yang, J.Y.H., et al. (2020). Transcriptional downregulation of MHC class I and melanoma de- differentiation in resistance to PD-1 inhibition. Nat Commun *11*, 1897. https://doi.org/10.1038/s41467-020-15726-7.

90. Izosimova, A.V., Shirmanova, M.V., Shcheslavskiy, V.I., Sachkova, D.A., Mozherov, A.M., Sharonov, G.V., Zagaynova, E.V., and Yuzhakova, D.V. (2022). FLIM of NAD(P)H in Lymphatic Nodes Resolves T-Cell Immune Response to the Tumor. International Journal of Molecular Sciences *23*, 15829. https://doi.org/10.3390/ijms232415829.

91. Yuzhakova, D.V., Sachkova, D.A., Izosimova, A.V., Yashin, K.S., Yusubalieva, G.M., Baklaushev, V.P., Mozherov, A.M., Shcheslavskiy, V.I., and Shirmanova, M.V. (2025). Fluorescence Lifetime Imaging of NAD(P)H in Patients' Lymphocytes: Evaluation of Efficacy of Immunotherapy. Cells *14*, 97. https://doi.org/10.3390/cells14020097.

92. Yang, M., Mahanty, A., Jin, C., Wong, A.N.N., and Yoo, J.S. (2022). Label-free metabolic imaging for sensitive and robust monitoring of anti-CD47 immunotherapy response in triple-negative breast cancer. J Immunother Cancer *10*, e005199. https://doi.org/10.1136/jitc-2022-005199.

93. Heaton, A.R., Burkard, N.J., Sondel, P.M., and Skala, M.C. (2024). Quantifying in vivo collagen reorganization during immunotherapy in murine melanoma with second harmonic generation imaging. Biophoton. Discovery *1*. https://doi.org/10.1117/1.BIOS.1.1.015004.

94. Perkins, N.D. (2004). NF-κB: tumor promoter or suppressor? Trends in Cell Biology *14*, 64–69. https://doi.org/10.1016/j.tcb.2003.12.004.

95. Hernández Borrero, L.J., and El-Deiry, W.S. (2021). Tumor suppressor p53: Biology, signaling pathways, and therapeutic targeting. Biochimica et Biophysica Acta (BBA) - Reviews on Cancer *1876*, 188556. https://doi.org/10.1016/j.bbcan.2021.188556.

96. Zhang, H., Kong, Q., Wang, J., Jiang, Y., and Hua, H. (2020). Complex roles of cAMP–PKA–CREB signaling in cancer. Experimental Hematology & Oncology *9*, 32. https://doi.org/10.1186/s40164-020-00191-1.

97. Elomaa, H., Ahtiainen, M., Väyrynen, S.A., Ogino, S., Nowak, J.A., Friman, M., Helminen, O., Wirta, E.-V., Seppälä, T.T., Böhm, J., et al. (2022). Prognostic significance of spatial and density analysis of T lymphocytes in colorectal cancer. Br J Cancer *127*, 514–523. https://doi.org/10.1038/s41416-022-01822-6.

98. Clark, P.J., and Evans, F.C. (1954). Distance to Nearest Neighbor as a Measure of Spatial Relationships in Populations. Ecology *35*, 445–453. https://doi.org/10.2307/1931034.

99. Yang, L., Zhang, W., Sun, J., Yang, G., Cai, S., Sun, F., Xing, L., and Sun, X. (2022). Functional status and spatial interaction of T cell subsets driven by specific tumor microenvironment correlate with recurrence of non-small cell lung cancer. Front Immunol *13*, 1022638. https://doi.org/10.3389/fimmu.2022.1022638.

100. Lopez de Rodas, M., Villalba-Esparza, M., Sanmamed, M.F., Chen, L., Rimm, D.L., and Schalper, K.A. (2025). Biological and clinical significance of tumour-infiltrating lymphocytes in the era of immunotherapy: a multidimensional approach. Nat Rev Clin Oncol *22*, 163–181. https://doi.org/10.1038/s41571-024-00984-x.

101. Schneider, C.A., Rasband, W.S., and Eliceiri, K.W. (2012). NIH Image to ImageJ: 25 years of image analysis. Nat Methods *9*, 671–675. https://doi.org/10.1038/nmeth.2089.

102. Becker, W. (2023). SPCImage NG Data Analysis Software. In The bh TCSPC handbook.

103. Pachitariu, M., and Stringer, C. (2022). Cellpose 2.0: how to train your own model. Nat Methods *19*, 1634–1641. https://doi.org/10.1038/s41592-022-01663-4.

104. Download — Python 3.13 documentation Python documentation. https://docs.python.org/3/download.html.

105. McGinnis, C.S., Murrow, L.M., and Gartner, Z.J. (2019). DoubletFinder: Doublet Detection in Single-Cell RNA Sequencing Data Using Artificial Nearest Neighbors. Cell Syst *8*, 329-337.e4. https://doi.org/10.1016/j.cels.2019.03.003.

106. Korsunsky, I., Millard, N., Fan, J., Slowikowski, K., Zhang, F., Wei, K., Baglaenko, Y., Brenner, M., Loh, P.-R., and Raychaudhuri, S. (2019). Fast, sensitive and accurate integration of single-cell data with Harmony. Nat Methods *16*, 1289–1296. https://doi.org/10.1038/s41592-019-0619-0.

107. Stuart, T., Butler, A., Hoffman, P., Hafemeister, C., Papalexi, E., Mauck, W.M., Hao, Y., Stoeckius, M., Smibert, P., and Satija, R. (2019). Comprehensive Integration of Single-Cell Data. Cell *177*, 1888-1902.e21. https://doi.org/10.1016/j.cell.2019.05.031.

108. Finak, G., McDavid, A., Yajima, M., Deng, J., Gersuk, V., Shalek, A.K., Slichter, C.K., Miller, H.W., McElrath, M.J., Prlic, M., et al. (2015). MAST: a flexible statistical framework for assessing transcriptional changes and characterizing heterogeneity in single-cell RNA sequencing data. Genome Biol *16*, 278. https://doi.org/10.1186/s13059-015-0844-5.

109. Stringari, C., Abdeladim, L., Malkinson, G., Mahou, P., Solinas, X., Lamarre, I., Brizion, S., Galey, J.-B., Supatto, W., Legouis, R., et al. (2017). Multicolor two-photon imaging of endogenous fluorophores in living tissues by wavelength mixing. Sci Rep *7*, 3792. https://doi.org/10.1038/s41598-017-03359-8.

110. Mahou, P., Zimmerley, M., Loulier, K., Matho, K.S., Labroille, G., Morin, X., Supatto, W., Livet, J., Débarre, D., and Beaurepaire, E. (2012). Multicolor two-photon tissue imaging by wavelength mixing. Nat Methods *9*, 815–818. https://doi.org/10.1038/nmeth.2098.

111. Conway, J.R.W., Warren, S.C., and Timpson, P. (2017). Context-dependent intravital imaging of therapeutic response using intramolecular FRET biosensors. Methods *128*, 78–94. https://doi.org/10.1016/j.ymeth.2017.04.014.

112. Seynhaeve, A.L.B., and ten Hagen, T.L.M. (2018). Intravital Microscopy of Tumor-associated Vasculature Using Advanced Dorsal Skinfold Window Chambers on Transgenic Fluorescent Mice. JoVE, 55115. https://doi.org/10.3791/55115.

113. Scheele, C.L.G.J., Herrmann, D., Yamashita, E., Lo Celso, C., Jenne, C.N., Oktay, M.H., Entenberg, D., Friedl, P., Weigert, R., Meijboom, F.L.B., et al. (2022). Multiphoton intravital microscopy of rodents. Nature Reviews Methods Primers *2*. https://doi.org/10.1038/s43586-022-00168-w.

114. Georgakoudi, I., and Quinn, K.P. (2023). Label-Free Optical Metabolic Imaging in Cells and Tissues. Annual Review of Biomedical Engineering *25*, 413–443. https://doi.org/10.1146/annurev-bioeng-071516-044730.

115. Ramanujam, N. (2000). Fluorescence Spectroscopy of Neoplastic and Non-Neoplastic Tissues. Neoplasia *2*, 89–117.

116. Alam, S.R., Wallrabe, H., Svindrych, Z., Chaudhary, A.K., Christopher, K.G., Chandra, D., and Periasamy, A. (2017). Investigation of Mitochondrial Metabolic Response to Doxorubicin in Prostate Cancer Cells: An NADH, FAD and Tryptophan FLIM Assay. Sci Rep *7*, 10451. https://doi.org/10.1038/s41598-017-10856-3.

117. Cao, R., Wallrabe, H., Siller, K., Rehman Alam, S., and Periasamy, A. (2019). Single-cell redox states analyzed by fluorescence lifetime metrics and tryptophan FRET interaction with NAD(P)H. Cytometry Part A *95*, 110–121. https://doi.org/10.1002/cyto.a.23711.

118. Hu, L., Wang, N., Cardona, E., and Walsh, A.J. (2020). Fluorescence intensity and lifetime redox ratios detect metabolic perturbations in T cells. Biomed Opt Express *11*, 5674–5688. https://doi.org/10.1364/BOE.401935.

119. Stringer, C., Wang, T., Michaelos, M., and Pachitariu, M. (2021). Cellpose: a generalist algorithm for cellular segmentation. Nat Methods *18*, 100–106. https://doi.org/10.1038/s41592-020-01018-x.

120. Guzman, E.C., Rehani, P.R., and Skala, M.C. (2023). Cell analysis tools: an open-source library for single-cell analysis of multi-dimensional microscopy images. In Imaging, Manipulation, and Analysis of Biomolecules, Cells, and Tissues XXI (SPIE), pp. 82–86. https://doi.org/10.1117/12.2647280.

121. Samimi, K., Desa, D.E., Pham, D.L., and Skala, M.C. (2025). ROI-summed analysis for improved fluorescence lifetime fitting accuracy and precision. In Multiphoton Microscopy in the Biomedical Sciences XXV (SPIE), p. PC1332412. https://doi.org/10.1117/12.3043430.

122. Sawilowsky, S.S. (2009). New Effect Size Rules of Thumb. Journal of Modern Applied Statistical Methods *8*, 597–599. https://doi.org/10.56801/10.56801/v8.i.452.

123. Gillette, A.A., Babiarz, C.P., VanDommelen, A.R., Pasch, C.A., Clipson, L., Matkowskyj, K.A., Deming, D.A., and Skala, M.C. (2021). Autofluorescence Imaging of Treatment Response in Neuroendocrine Tumor Organoids. Cancers *13*, 1873. https://doi.org/10.3390/cancers13081873.

STAR★METHODS

KEY RESOURCES TABLE

REAGENT OR RESOURCE	SOURCE	IDENTIFIER
Antibodies		
Rat monoclonal anti-CD8α (clone 2.43)	BioXcell	Cat#BE0061; RRID: AB_1125541
Rat monoclonal anti-CD4 (clone GK1.5)	BioXcell	Cat#BE0003-1; RRID: AB_1107636
Mouse monoclonal NK1.1 (clone PK136)	BioXcell	Cat#BE0036; RRID: AB_1107737
Normal rat IgG	Sigma-Aldrich	Cat#NI04-100UG
Rat monoclonal FITC anti-CD45 (clone 30-F11)	BioLegend	Cat#103108; RRID: AB_312973
Rat monoclonal Brilliant Violet 510 anti-CD45 (clone 30-F11)	BioLegend	Cat#103138; RRID: AB_2563061
Rat monoclonal Brilliant Violet 605 anti-CD45 (clone 30-F11)	BioLegend	Cat#103140; RRID: AB_2562342
Rat monoclonal PE/Cyanine5 anti-CD3 (clone 17A2)	BioLegend	Cat#100274; RRID: AB_2894410
Mouse monoclonal Brilliant Violet 510 anti-NK1.1 (clone PK136)	BioLegend	Cat#108738; RRID: AB_2562217
Mouse monoclonal PE/Dazzle 594 anti-NK1.1 (clone PK136)	BioLegend	Cat#108748; RRID: AB_2564219
Mouse monoclonal Brilliant Violet 605 anti-NK1.1 (clone PK136)	BioLegend	Cat#108753; RRID: AB_2686977
Rat monoclonal Brilliant Violet 605 anti-CD8α (clone 53-6.7)	BioLegend	Cat#100744; RRID: AB_2562609

Rat monoclonal APC-R700 anti-CD8α (clone 53-6.7)	BD Biosciences	Cat#564983; RRID: AB_2739032
Rat monoclonal Brilliant Violet 711 anti-CD8a (clone 53-6.7)	BioLegend	Cat#100748; RRID: AB_2562100
Rat monoclonal Alexa Fluor 700 anti-CD4 (clone GK1.5)	BioLegend	Cat#100430; RRID: AB_493699
Rat monoclonal PE anti-CD4 (clone GK1.5)	BioLegend	Cat#100408; RRID: AB_312693
Rat monoclonal FITC anti-CD4 (clone GK1.5)	BioLegend	Cat#100406; RRID: AB_312691
Rat monoclonal PE/Dazzle 594 anti-CD19 (clone 6D5)	BioLegend	Cat#115554; RRID: AB_2564001
Rat monoclonal APC anti-CD19 (clone 6D5)	BioLegend	Cat#115512; RRID: AB_313647
Rat monoclonal BD Horizon V450 anti-CD11b (clone M1/70)	BD Biosciences	Cat#560455; RRID: AB_1645266
Rat monoclonal BD Horizon Brilliant Blue 700 anti-CD11b (clone M1/70)	BD Biosciences	Cat#566416; RRID: AB_2744272
Armenian hamster monoclonal Alexa Fluor 700 anti-CD11c (clone N418)	BioLegend	Cat#117320; RRID: AB_528736
Rat monoclonal PE/Cy7 anti-F4/80 (clone BM8)	BioLegend	Cat#123114; RRID: AB_893478
Rat monoclonal PE anti-Ly-6G (clone 1A8)	BioLegend	Cat#100406; RRID: AB_1186099
Rat monoclonal Brilliant Violet 421 anti-CD107a (clone 1D4B)	BioLegend	Cat#121618; RRID: AB_2749905
Rat monoclonal PE anti-Perforin (clone S16009A)	BioLegend	Cat#154306; RRID: AB_2721639
Rat monoclonal PE/Cyanine7 anti-IFNγ (clone XMG1.2)	BioLegend	Cat#505826; RRID: AB_2295770
Rat monoclonal Brilliant Violet 711 anti-IFNγ (clone XMG1.2)	BioLegend	Cat#505836; RRID: AB_2650928
Rat monoclonal APC anti-Granzyme B (clone QA18A28)	BioLegend	Cat#396408; RRID: AB_2801077
Armenian hamster monoclonal Brilliant Violet 510 anti-CD69 (H1.2F3)	BioLegend	Cat#104532; RRID: AB_2562327
Rat monoclonal Brilliant Violet 421 anti-CD279 (PD-1) (clone 29F.1A12)	BioLegend	Cat#135221; RRID: AB_2562568
Rat monoclonal Brilliant Violet 711 anti-CD223 (LAG-3) (clone C9B7W)	BioLegend	Cat#125243; RRID: AB_2876450
Rat monoclonal APC anti-CD366 (TIM-3) (clone RMT3-23)	BioLegend	Cat#119706; RRID: AB_256656
Mouse monoclonal Brilliant Violet 605 anti-TIGIT (Vstm3) (clone 1G9)	BioLegend	Cat#142121; RRID: AB_3083126
Rat monoclonal TruStain FcX PLUS anti-CD16 / CD32 (clone S17011E)	BioLegend	Cat#156604; RRID: AB_2783138
Rat monoclonal CD16 / CD32 (Fc Shield) (clone 2.4G2)	Tonbo (now Cytek Biosciences)	Cat#70-0161-M001; RRID:AB_2621487
Rabbit monoclonal anti-CD4 (clone EPR19514)	Abcam	Cat#ab183685; RRID: AB_2686917
Rabbit monoclonal anti-CD8α (clone EPR21769)	Abcam	Cat#ab217344; RRID: AB_2890649

Rabbit monoclonal anti-CD161 (clone EPR21236)	Abcam	Cat#ab234107; RRID: AB_2922430
Rat monoclonal anti-perforin (clone CB5.4)	Abcam	Cat#ab16074; RRID: AB_302236
Rabbit monoclonal anti-SOX10 (clone SP267)	Abcam	Cat#ab227680; RRID: AB_2927464
Rabbit monoclonal anti-cleaved PARP-1 (clone E51)	Abcam	Cat#ab32064
Rabbit monoclonal anti-CD3 (clone SP162)	Abcam	Cat#ab135372; RRID: AB_2884903
Rabbit monoclonal anti-CD19 (clone EPR23174-145)	Abcam	Cat#ab245235; RRID: AB_2895109
Rat monoclonal anti-F4/80 (clone CI:A3-1)	Abcam	Cat#ab6640
Rabbit polyclonal anti-CD69	Abcam	Cat#ab202909; RRID: AB_2889247
Rabbit polyclonal anti-mCherry	Abcam	Cat#ab167453; RRID: AB_2571870
Goat polyclonal anti-rabbit IgG H&L (HRP) preadsorbed	Abcam	Cat#ab7090; RRID: AB_955417
Goat polycloncal anti-rat IgG H&L (HRP) preadsorbed	Abcam	Cat#ab7097; RRID: AB_955411
Chemicals, peptides, and recombinant proteins		
Donor Sequence: mCherry-CD8.Megamer CCTCCCCCACCGCACCTCCTCCGCCCTGTTCCTGGGCCCCTCCC CTAGAGCCCTAGCTTGACCTAAGCTGCTTGCTGGTGGAGAGCAC ACCATGGTGAGCAAGGGCGAGGAGGATAACATGGCCATCATCAA GGAGTTCATGCGCTTCAAGGTGCACATGGAGGGCTCCGTGAACG GCCACGAGTTCGAGATCGAGGGCGAGGGCGAGGGCCGCCCCTA CGAGGGCACCCAGACCGCCAAGCTGAAGGTGACCAAGGGTGGC CCCCTGCCCTTCGCCTGGGACATCCTGTCCCCTCAGTTCATGTAC GGCTCCAAGGCCTACGTGAAGCACCCCGCCGACATCCCCGACTA CTTGAAGCTGTCCTTCCCCGAGGGCTTCAAGTGGGAGCGCGTGA TGAACTTCGAGGACGGCGGCGTGGTGACCGTGACCCAGGACTC CTCCCTGCAGGACGGCGAGTTCATCTACAAGGTGAAGCTGCGCG GCACCAACTTCCCCTCCGACGGCCCCGTAATGCAGAAGAAGACC ATGGGCTGGGAGGCCTCCTCCGAGCGGATGTACCCCGAGGACG GCGCCCTGAAGGGCGAGATCAAGCAGAGGCTGAAGCTGAAGGA CGGCGGCCACTACGACGCTGAGGTCAAGACCACCTACAAGGCCA AGAAGCCCGTGCAGCTGCCCGGCGCCTACAACGTCAACATCAAG TTGGACATCACCTCCCACAACGAGGACTACACCATCGTGGAACA GTACGAACGCGCCGAGGGCCGCCACTCCACCGGCGGCATGGAC GAGCTGTACAAGGCCACGAACTTCTCTCTGTTAAAGCAAGCAGGA GACGTGGAAGAAAACCCCGGTCCTATGGCCTCACCGTTGACCCG CTTTCTGTCGCTGAACCTGCTGCTGCTGGGTGAGTCGATTATCCT GGGGAGTGGAGAAGCTAAGCCACAGGCACCCGAA	IDT	
Primer: 1033 | Nterm.F.ILTS.1 TTGCTCTGCAAGGGTGCATTC	IDT	
Primer: 1185 | mScarlet.R.2 TCCTCGTTGTGGGAGGTGATGTCC	IDT	
Primer: 1034 | Nterm.R.1.ILTS ACCAGGTCCACCTTCTGACCAAG	IDT	
Primer: 800 | 000D.mCherry.F.1 CAAGTGGGAGCGCGTGATG	IDT	
Target sequence: sgRNA.M1.2 TGCTGGTGGAGAGCACACCATGG	IDT	
ACK lysis buffer	Gibco	Cat#A10492-01
Collagenase type IV	Gibco	Cat#17104019
DNase I	Sigma Aldrich	Cat#DN25
Protein transport inhibitor	eBioscience	Cat#00-4980-03
Ghost Dye Red 780 viability dye	Tonbo Biosciences	Cat#13-0865-T500

BD Horizon brilliant stain buffer	BD Biosciences	Cat#563794
Fixation / Permeabilization buffer	eBioscience	Cat#00-5523-00
Cyto-Fast Fixation / Permeabilization Buffer Set	BioLegend	Cat#426803
10X AR9	Akoya Biosciences	Cat#AR900250ML
1X Antibody Diluent / Block Solution	Akoya Biosciences	Cat#ARD1001EA
1X Amplification Diluent	Akoya Biosciences	Cat#FP1498
Prolong Gold Antifade Reagent	Invitrogen	Cat#P36930
DAPI	Akoya Biosciences	Cat#FP1490
Opal 520	Akoya Biosciences	Cat#FP1487001KT
Opal 540	Akoya Biosciences	Cat#FP1494001KT
Opal 570	Akoya Biosciences	Cat#FP1488001KT
Opal 620	Akoya Biosciences	Cat#FP1495001KT
Opal 650	Akoya Biosciences	Cat#FP1496001KT
Opal 690	Akoya Biosciences	Cat#FP1497001KT
Critical commercial assays		
EasySep Mouse T Cell Isolation Kit	STEMCELL Technologies	Cat#19851
Tumor Dissociation Kit	Miltenyi	Cat#130-096-730
Dead Cell Removal Kit	Miltenyi	Cat#130-090-101
Chromium Next GEM Single Cell 5' Reagent Kit v2	10X Genomics	Cat#1000263
High Sensitivity D5000 ScreenTape	Agilent	Cat#5067-5588
Deposited data		
Raw and analyzed optical metabolic imaging data	This paper	
Raw and analyzed flow cytometry data	This paper	
Raw and analyzed scRNAseq data	Erbe *et al.*[19]	
Experimental models: Cell lines		
Mouse: B78-D14 cells	Ralph Reisfeld, Scripps Research Institute	
Mouse: MC-38 cells	Brad St. Croix, NIH	RRID:CVCL_B288
Experimental models: Organisms/strains		
Mouse: CD8-mCherry	This paper	
Mouse: C57BL/6J; strain #000664	The Jackson Laboratory	RRID:IMSR_JAX:000664
Mouse: C57BL/6NTac	Taconic Biosciences	RRID:IMSR_TAC:B6
Software and algorithms		
ImageJ	Schneider *et al.* [101]	https://imagej.net/ij/
SPCImage NG Data Analysis Software (v 8.1)	Becker [102]	https://www.becker-hickl.com/products/spcimage/
Cellpose2.0	Pachitariu [103]	https://github.com/MouseLand/cellpose
Python (v3.10.12)	Python documentation [104]	https://www.python.org/
FlowJo (v10.7.1)	BD	https://www.flowjo.com/

Cell Ranger (v3)	10X Genomics	https://www.10xgenomics.com/support/software/cell-ranger/latest
DoubletFinder	McGinnis *et al.* [105]	https://github.com/chris-mcginnis-ucsf/DoubletFinder
Harmony	Korsunsky *et al.* [106]	https://github.com/immunogenomics/harmony
Seurat	Stuart *et al.* [107]	https://satijalab.org/seurat/
Clustree	CRAN	https://github.com/lazappi/clustree
MAST	Finak *et al.* [108]	https://rglab.github.io/MAST/
R (v4)	CRAN	https://www.r-project.org/
SAS (v9.4)	SAS Institute	https://www.sas.com/en_us/home.html
Prism (v10.4)	GraphPad	https://www.graphpad.com/features
Other		
Rainbow beads	Spherotech	Cat#RFP-30-5A
Sphero Rainbow Fluorescent Particles, 3.0-3.4 µm (mid-range FL1 fluorescence)	BD Biosciences	Cat#556298
UltraComp eBeads Plus Compensation Beads	Invitrogen	Cat#01-3333-42
70 µm nylon filter	Corning	Cat#352350
40 µm nylon filter	Corning	Cat#352340
gentleMACS C tubes	Miltenyi	Cat#130-093-237

EXPERIMENTAL MODEL AND STUDY PARTICIPANT DETAILS

Cell lines

B78-D14 (B78) melanoma is a poorly immunogenic mouse cell line derived from B78-H1 melanoma cells, which were originally derived from B16 melanoma. These cells were obtained from Ralph Reisfeld (Scripps Research Institute) in 2002. B78 cells were transfected with functional GD2/GD3 synthase to express the disialoganglioside GD2, which is overexpressed on the surface of many human tumors including melanoma. These B78 cells were also found to lack melanin. MC38 is a mouse colon adenocarcinoma cell line. These cells were obtained from Brad St. Croix (NIH). B78 and MC38 cells were grown in RPMI-1640 (Gibco) supplemented with 10% FBS and 1% penicillin/ streptomycin; B78 media was periodically supplemented with 400 µg G418 and 500 µg Hygromycin B per mL. Mycoplasma testing was performed every 6 months.

Animal models

C57BL/6J mice were obtained from Jackson Laboratories. C57BL/6NTac were obtained from Taconic Biosciences. The mCherry-CD8α knock-in mouse (CD8-mCherry) was designed and generated by the University of Wisconsin-Madison Genome Editing (RRID:SCR_021070) and Animal Model (RRID:SCR_024797) Cores. Pronuclear microinjection was conducted into C57BL/6J embryos using a mixture of Cas9 protein, a long single-stranded donor template (IDT, Megamer ssDNA Fragment), and an *in vitro* transcribed sgRNA (TGCTGGTGGAGAGCACACCATGG) targeting the N-terminus of the CD8α coding sequence. The mCherry-P2A knock-in cassette resulted in a CD8 reporter allele, rather than an mCherry-CD8 fusion. Pups were sequenced using primers 1033 and 1185 (N-terminal) and 1034 and 800

(C-terminal) followed by Sanger sequencing. A sequence-confirmed founder was identified, the founder was backcrossed to C57BL/6J to produce F1 progeny, and F1 progeny were similarly sequence confirmed. Animals used were 8-24 weeks of age. All animal work was performed under an animal protocol approved by the Institutional Animal Care and Use Committee at the University of Wisconsin, Madison. A maximum of 5 mice were housed per cage. Standard chow and water were provided *ad libitum*. Enrichment (nesting material and igloo) was provided to all cages. Male and female mice were used for all experiments.

METHOD DETAILS

Mouse tumor model preparation and therapy administration

2×10^6 B78 cells were injected intradermally (I.D.) into the right flank in a volume of 0.1 mL PBS. 5×10^5 MC38 cells were injected I.D. into the right flank in a volume of 0.1 mL PBS. For the GD2+ B78 model, mice were randomized into treatment groups when tumors reached enrollment size (~150 mm^3), which typically required 3 to 4 weeks of *in vivo* growth. For the GD2- MC38 model, mice were randomized into treatment groups when tumors reached enrollment size (~150 mm^3), which typically required 7 to 10 days of *in vivo* growth. Each randomized group included male and female mice, where the average tumor size of each group was matched. The first day of treatment is defined here as "day 0". For both B78 and MC38 mice, external beam radiation therapy was delivered to the tumor surface of treated mice only on day 0, using an X-RAD 320 cabinet irradiator system (Precision X-Ray, North Branford, Connecticut, United States). Mice were immobilized using custom lead jigs that exposed only the dorsal right flank. Radiation was delivered in one fraction to a maximum dose of 12 Gray (Gy). For both B78 and MC38 mice, systemic mouse α-CTLA-4 antibody was administered to treated mice once daily on days 2, 5, and 8 via intraperitoneal injections of 200 µg in 200 µL PBS (Bristol-Meyers Squibb, Redwood City, California, United States and NeoClone Biotechnologies International, Madison, Wisconsin, United States). For B78 mice only, Hu14.18-IL2 immunocytokine, a monoclonal anti-GD2 antibody fused to IL-2 cytokine, was administered to treated mice once daily on days 5 to 9 via intratumoral injections of 50 µg in 100 µL PBS (AnYxis Immuno-Oncology GmbH, Vienna, Austria). For MC38 mice only, IL-2 cytokine was administered to treated mice once daily on days 5 to 9 via intratumoral injections of 75,000 IU in 100 µL PBS (Hoffman-La Roche, Basel, Switzerland). Vehicle-treated mice were injected once daily on days 2, 5, and 8 via intraperitoneal injections of 200 µL PBS and once daily on days 5 to 9 via intratumoral injections of 100 µL PBS. No external beam radiation therapy was administered to vehicle-treated mice. Pretreatment mice received no PBS or immunotherapy injections and no external beam radiation therapy. Tumor growth was monitored via caliper measurements. Tumor volumes were calculated as such: $(\text{width}^2 \times \text{length}) / 2$. All tumor efficacy and survival experiments in both B78 and MC38 models were completed in CD8-mCherry and C57BL/6J mice. Three experimental repeats were completed for both B78 and MC38 tumor models.

Mouse rechallenge studies

At least two months after treated mice were cured, tumor rechallenge studies were performed. For the B78 model, 2×10^6 B78 cells were injected I.D. into the right abdomen of both cured / memory mice and age-matched naïve mice. For the MC38 model, 5×10^5 MC38 cells were injected I.D. into the right abdomen of both cured / memory mice and age-matched naïve mice. No treatment was given to either cured / memory mice or naïve mice. Tumor growth was monitored via caliper measurements. Tumor volumes were calculated as such: $(\text{width}^2 \times \text{length}) / 2$. All rechallenge experiments in both B78 and MC38 models were completed in CD8-mCherry and C57BL/6J mice. Three experimental repeats were completed for both B78 and MC38 tumor models.

Mouse immune depletion studies

For the B78 model, C57BL/6J mice were used for immune depletion studies. CD8 T cells were depleted via anti-CD8 antibody (clone 2.43, BioXcell) at 50 µg in 0.5 mL PBS per dose on days -2, 2, 5, 8, 12, 15, 18, 22. CD4 T cells were depleted via anti-CD4 antibody (clone GK1.5, BioXcell) at 200 µg in 0.5 mL PBS per dose on days -2, 5, 12, 18. NK cells were depleted via anti-NK1.1 antibody (clone PK136, BioXcell) 200 µg in 0.5 mL PBS per dose on days -2, 2, 5, 8, 12, 15, 18, 22. Control mice received normal rat IgG antibody (Sigma-Aldrich) 200 µg in 0.5 mL PBS per dose on days -2, 2, 5, 8, 12, 15, 18, 22. Flow cytometry of peripheral blood was performed to confirm antibody depleted was successful. For the MC38 model,

C57BL/6NTac mice were used for immune depletion studies. CD8 T cells were depleted via anti-CD8 antibody (BioXcell) at 50 µg in 0.5 mL PBS per dose on days -1, 6, 13, 20. CD4 T cells were depleted via anti-CD4 antibody (BioXcell) at 200 µg in 0.5 mL PBS per dose on days -1, 6, 13, 20. NK cells were depleted via anti-NK1.1 antibody (BioXcell) 200 µg in 0.5 mL PBS per dose on days -1, 6, 13, 20. One experimental replicate was completed for B78 model and two biological replicates were completed for MC38 tumor model. Statistical comparison of different immune depleted mouse groups is color-coded for each comparison (**Figure 1, 3**).

Multiphoton imaging in vitro

In vitro imaging of CD3+ T cells was performed by negative isolation of splenic T cells (STEMCELL Technologies) from a C57BL/6J mouse and CD8-mCherry reporter mouse using an EasySep Mouse T Cell Isolation Kit. Isolated T cells were plated in a PBS droplet on coated glass imaging dishes, allowed to settle for 2 hours, and then imaged the same day. Autofluorescence images were captured with a custom-built multi-photon microscope (Bruker) using an ultrafast femtosecond laser (InSight DSC, Spectra Physics). Autofluorescence images were captured with a custom-built multi-photon microscope (Bruker) using an ultrafast femtosecond laser (InSight DSC, Spectra Physics). Fluorescence lifetime measurements were performed using time-correlated single photon counting electronics (Becker & Hickl). Fluorescence emission, in FLIM mode, was detected simultaneously in three channels using bandpass filters of 466/40 nm (NAD(P)H), 514/30 nm (FAD), and 650/45 nm (mCherry) prior to detection with three GaAsP photomultiplier tubes (Hamamatsu). All three fluorophores were simultaneously excited using a previously reported wavelength mixing approach.[66,109,110] During wavelength mixing in FLIM mode, typical power at the power meter was ~0.3-0.7 mW for the 750 nm laser and ~1.1-1.8 mW for the 1041 laser. All images were acquired with a 40×/1.13 NA water-immersion objective (Nikon) at 512×512pixel resolution and an optical zoom of 1.0-2.0. NAD(P)H, FAD, and mCherry intensity and lifetime images were acquired across 6 fields of view. One biological replicate was performed.

In vitro imaging of B78 and MC38 tumor cells was performed by plating 100,000-150,000 tumor cells in RPMI-1640 media, on coated glass imaging dishes (2 technical replicates) 48 hours prior to imaging. To inhibit oxidative phosphorylation / electron transport chain complex IV, cells were first imaged untreated, then treated with 4 mM sodium cyanide (NaCN) in PBS, then imaged again 15 minutes post-treatment. To inhibit glycolysis, cells were first imaged untreated, then treated with 10 mM 2-Deoxy-D-glucose (2DG) in PBS, then imaged again 2 hours post-treatment. B78 and MC38 cells were imaged for two experimental repeats for each inhibitor treatment. Autofluorescence images were captured with a custom-built multi-photon microscope (Bruker) using an ultrafast femtosecond laser (InSight DSC, Spectra Physics). The laser was tuned to 750 nm for NAD(P)H excitation and tuned to 890 nm for FAD excitation. The average power at the power meter was ~2-3.5 mW for NAD(P)H excitation and ~4-4.5 mW for FAD excitation. A pixel dwell time of 4.8 µs was used for all images. NAD(P)H and FAD images were acquired sequentially. A 440/80 nm bandpass filter isolated NAD(P)H emission onto the photomultiplier tube (PMT) detector. A dichroic mirror directed wavelengths greater than 500 nm onto a 550/100 nm bandpass filter, isolating FAD emission onto a second PMT. Fluorescence lifetime measurements were acquired with time-correlated single photon counting electronics (Becker and Hickl) and a GaAsP PMT (Hamamatsu). All images were acquired with a 40×/1.13 NA water-immersion objective (Nikon) at 512×512 pixel resolution and an optical zoom of 1.0. NAD(P)H and FAD intensity and lifetime images were acquired to sample metabolic behavior of B78 and MC38 tumor cells across 4-5 fields of view per dish, per condition. Two experimental repeats were performed for both B78 and MC38.

Multiphoton imaging in vivo

All imaging experiments were completed in CD8-mCherry mice. Intravital imaging of mouse B78 tumors was performed in pretreatment mice (n = 4), vehicle-treated mice (n = 6), and treated mice (n = 6) across days 0, 6, 9, and 12 of therapy. Intravital imaging of mouse MC38 tumors was performed on pretreatment mice (n = 4), vehicle-treated mice (n = 4), and treated mice (n = 4) across days 0, 6, and 9 of therapy. Imaged mice for all work were 50% male and 50% female. Day 0 images, the pretreatment group, are used as a baseline comparison for both vehicle and radioimmunotherapy-treated groups. Immediately prior to

tumor imaging, skin flap surgery exposed flank tumors as previously reported.[68,93,111–113] Mice were anesthetized with isoflurane, and then, the skin around the tumor was cut into a flap and separated from the body cavity so that the tumor laid flat on the imaging stage while still connected to the vasculature. Mice were placed on a specialized microscope stage for imaging and kept in a heating chamber (air maintained at 37°C) during imaging. An imaging dish insert and PBS for coupling were used with surgical tape to secure skin flap tumors. All imaging experiments were terminal, with new mice being imaged at each time point. The skin flap method allowed easy tumor access for intratumoral immunotherapy administration on days 5 to 9 and eliminated the concern of an immune response related to the flank window method.

Autofluorescence images were captured with a custom-built multi-photon microscope (Bruker) using an ultrafast femtosecond laser (InSight DSC, Spectra Physics). Fluorescence lifetime measurements were performed using time-correlated single photon counting electronics (Becker & Hickl). Fluorescence emission, in FLIM mode, was detected simultaneously in three channels using bandpass filters of 466/40 nm (NAD(P)H), 514/30 nm (FAD), and 650/45 nm (mCherry) prior to detection with three GaAsP photomultiplier tubes (Hamamatsu). All three fluorophores were simultaneously excited using a previously reported wavelength mixing approach.[66,109,110] During wavelength mixing in FLIM mode, typical power at the power meter was ~0.8-2.2 mW for the 750 nm laser and ~1.5-3.2 mW for the 1041 laser. All images were acquired with a 40×/1.13 NA water-immersion objective (Nikon) at 512×512pixel resolution and an optical zoom of 1.0-2.0. NAD(P)H, FAD, and mCherry intensity and lifetime images were acquired to sample metabolic behavior of B78 and MC38 tumor as well as CD8 T cells across 5-11 fields of view and multiple depths within each tumor. Within **Figure 2B, 4B** the *in vivo* multiphoton images shown in top, middle, and bottom rows are the identical fields of view represented in three different ways: intensity, free NAD(P)H α_1, and protein-bound FAD α_1. Two experimental repeats were performed for both B78 and MC38.

Multiphoton image analysis

The fluorescence lifetimes of free and protein-bound NAD(P)H and FAD are distinct, and these lifetimes along with their weights can be recovered with a two-exponential fit function. Therefore, fluorescence lifetime decays for both NAD(P)H and FAD were fit to the following bi-exponential function in SPCImage (v8.1):

$$I(t) = \alpha_1 e^{-t/\tau_1} + \alpha_2 e^{-t/\tau_2} + C$$

For NAD(P)H, τ_1 corresponds to the free lifetime, τ_2 corresponds to the protein-bound lifetime, and the weights (α_1, α_2; $\alpha_1 + \alpha_2 = 1$) correspond to the proportion of free and protein-bound NAD(P)H, respectively.[59,60,62,63,114] Conversely for FAD, τ_1 corresponds to the protein-bound lifetime and τ_2 corresponds to the free lifetime.[63,65,115] An instrument response function was measured using SHG (900 nm excitation) from urea crystals for input into the decay fit procedure. The following fluorescence lifetime endpoints were calculated from the fitted model: τ_1, τ_2, α_1, and α_2 for both NAD(P)H and FAD; along with the fluorescence lifetime redox ratio (FLIRR): NAD(P)H a2 / FAD a1 (**Table S1**).[59,60,64,65,114,116–118]

Automated cell segmentation was performed through Cellpose2.0, with manual corrections made as needed using the Napari viewer through a custom Python script.[103,119] Single tumor cells were identified, circled, and segmented as whole cells (nuclei and cytoplasm captured) using NAD(P)H intensity images. Single CD8 T cells were identified, circled, and segmented as whole cells using mCherry intensity images. The resulting segmented images were saved as masks. Using these masks and the raw imaging data, fluorescence lifetime variables and FLIRR values were calculated for each individual cell using custom code adapted from Cell Analysis Tools.[120] Fluorescence lifetime variables were calculated on a region of interest or cell level, with a single decay curve for each individual cell.[121] Receiver operator characteristic (ROC) curves were generated using a random forest algorithm. These ROC curves classified CD8 T cell and tumor cell population based on treatment conditions. **Table S1** shows metabolic and morphological parameters included in the algorithm; 50% train: 50% test. Calculations were performed using Python (v3.10.12) / Spyder.

Flow cytometry sample preparation and acquisition

All flow cytometry experiments were completed in CD8-mCherry mice. At each treatment timepoint, mice were euthanized with CO_2, and tumors and spleens were excised. Spleens were manually disaggregated and filtered with a 70 µm filter (Corning), resulting in a single cell suspension. Red blood cell lysis was performed on spleens with ACK lysis buffer (Gibco) or water. Tumors were first manually disaggregated in petri dishes by chopping into ~1 mm pieces using a scalpel. Tumors were transferred to 50 mL conical tubes containing 2.5-5 mL of complete RPMI (Gibco), 2.5 mg of collagenase type IV, 250 µg of DNase, and 1X protein transport inhibitor (PTI, eBioscience). Samples were further disaggregated by placing on a heated shaker at 37°C for 45 minutes or placed on a gentleMACS Octo Dissociator using program 37C_m_TDK1. Final single cell suspensions of tumor samples were obtained by passing through a 70 µm filter. Tumor and spleen samples were resuspended in flow buffer (PBS + 2% fetal bovine serum) plus 1X PTI, kept on ice, and protected from light for 4-6 hours. 3×10^6 cells from each individual tumor or spleen sample were added to individual 5 mL flow tubes. Leftover cells were pooled and used for fluorescence minus one controls. For the live/dead control, 1.5×10^6 cells were killed via heat shock and mixed with 1.5×10^6 live cells. Samples were resuspended in PBS plus PTI and stained with Ghost Dye Red 780 (Tonbo Biosciences) for 30 minutes at 4°C, protected from light. After being washed with flow buffer plus PTI, samples were incubated with anti-CD16/32 (BioLegend or Tonbo Biosciences) for 5 minutes at room temperature to reduce nonspecific binding. Samples were stained with surface antibodies in brilliant stain buffer (BD Biosciences) for 30 minutes at 4°C, protected from light. For samples including intracellular markers, cells were washed with flow buffer plus PTI and fixed with Fixation/Permeabilization buffer (eBioscience) for 30 minutes at 4°C, protected from light. After being washed with 1X permeabilization buffer, samples were stained with intracellular antibodies in permeabilization buffer overnight at 4°C, protected from light. The following day, samples were washed once with permeabilization buffer and once with flow buffer. Samples were acquired on an Attune NxT flow cytometer (Thermo Fisher). The following surface antibodies were used: CD45 FITC or BV510 or BV605, CD3 PE-Cy5, NK1.1 BV510 or PE-Dazzle 594 or BV605, CD8α BV605 or APC-R700 or BV711, CD4 AlexaFluor700 or PE or FITC, CD19 PE-Dazzle 594 or APC, CD11b BD Horizon V450 or BD Horizon BB700, CD11c AlexaFluor700, F4/80 PE-Cy7, Ly-6G PE, CD107a BV421, PD-1 BV421, LAG-3 BV711, TIM-3 APC, TIGIT BV605, CD69 BV510 (BioLegend or BD Biosciences). The following intracellular antibodies were used: Perforin PE, IFNγ PE-Cy7 or BV711, GzmB APC (all from BioLegend). Two to four experimental repeats were completed to characterize immune infiltrate populations, activation, effector function, and exhaustion for both B78 and MC38 tumors across time via flow cytometry.

Flow cytometry data analysis

Data were standardized between timepoints using rainbow beads (Spherotech). Data were analyzed using FlowJo (v10.7.1) and gates were determined using fluorescent minus one controls. At least one C57BL/6 non-mCherry mouse was included in each study to assist in setting mCherry gates.

scRNAseq sample preparation and acquisition

Details on sample preparation and acquisition can be found at Erbe *et al.*[19]

scRNAseq analysis of CD8 T, CD4 T, NK, and B78 tumor cells from B78 tumors treated with radio-immunotherapy

We utilized our scRNAseq data of B78 tumors, generated from an independent study,[19] to evaluate metabolic genes and pathways in CD8 T, CD4 T, NK, and B78 tumor cells from vehicle and treated tumors. We used *Sox10* to select out tumor cells, *Cd4* for CD4+ T cells, *Cd8a* for CD8+ T cells, and *Ncr1* for NK cells for further clustering to determine subsets within each compartment. To account for potential technical variance across samples, we used a fuzzy clustering-based integration method (Harmony method).[106] Downstream analysis for CD8 T cells and B78 tumor cells were based on Seurat single-cell analysis package[107] including: graph-based clustering based on 20 Principal Components using *FindCluster* with different resolution from 0.1 to 2 to determine the number of clusters based on representative markers overlaid in the hierarchical tree across different resolution (Clustree R package), differential expression analysis using MAST[108] implemented in Seurat with the cutoff average log2FC 0.25, adjusted *p*-value cutoff

of 0.01, and at least 20% of cells expressing the markers. Visualization with UMAPs, heatmaps, dot plots, and violin plots was done using Seurat in R (v4.4.2) and the Bioconductor platform. Metabolism pathway and immune functional signature was calculated as the average of the genes in the Mouse Kyoto Encyclopedia of Genes and Genomes (KEGG)[75–77] metabolism for each cell subset.

Multiplex immunofluorescence sample preparation and acquisition

All multiplex immunofluorescence experiments were completed in CD8-mCherry mice with C57BL/6J tissues included as controls. To characterize CD8-mCherry mice, untreated B78 tumors and spleens were excised, formalin fixed, and paraffin-embedded (FFPE) for antibody staining with a panel of fluorescent markers (CD4, CD8α, mCherry) (all from Abcam) (**Figure S1**). Embedded sections were deparaffinized and hydrated prior to 7 min microwave antigen retrieval using 10X AR9 (Akoya Biosciences) diluted 1:10 with dH_2O, a high pH antigen retrieval buffer, and placement in 1X Antibody Diluent / Block Solution (Akoya Biosciences) for 10 min at RT. Next, primary antibodies were sequentially applied upon removal of blocking solution at the following dilutions and incubation times: CD4 – 1:500 for 15 min, CD8α –1:250 for 15 min, mCherry 1:500 – for 10 min. Following 1X tris-buffered saline washes, ~200 µL diluted rat or rabbit secondary antibody (Abcam) was applied to each slide and incubated for 10 min. Following a 1X tris-buffered saline wash, Opal dyes were applied at 1:100 dilution for 10 min in 1X Amplification Diluent (Akoya Biosciences): (tumor and spleen sections) CD4 – Opal-dye 520, CD8α – Opal dye 620, mCherry – Opal dye 570 (all from Akoya Biosciences). Finally, stained sections were incubated in diluted DAPI (Akoya Biosciences) for 10 min at RT for nuclear labeling and mounted on glass coverslips with Prolong Gold Antifade Reagent (Invitrogen) for imaging. Imaging was performed on whole tumor and spleen slides at 4× and then regions of interest (ROIs) were selected and imaged at 20× using a Vectra multispectral imaging system (Akoya Biosciences). One experimental replicate was performed.

For all other studies using treated and vehicle CD8-mCherry mice, excised B78 tumors were formalin fixed and paraffin-embedded for antibody staining with a panel of fluorescent markers (perforin, SOX10, CD161, cPARP-1, CD4, CD8α) (all from Abcam). Two tumors were embedded per paraffin block. Excised spleens and lymph nodes from B78 tumor bearing mice were formalin fixed and processed into FFPE blocks. 2.5 mm cores were punched from these donor blocks to create a tissue microarray (TMA) to fit samples from this study cohort. This mouse TMA was stained with a panel of fluorescent markers (F4/80, CD69, CD19, CD3, CD4, CD8α) (all from Abcam) (**Figures 7, S6**). Embedded sections were deparaffinized and hydrated prior to 7 min microwave antigen retrieval using 10X AR9 (Akoya Biosciences) diluted 1:10 with dH_2O, a high pH antigen retrieval buffer, and placement in 1X Antibody Diluent / Block Solution (Akoya Biosciences) for 10 min at RT. Next, primary antibodies were sequentially applied upon removal of blocking solution at the following dilutions and incubation times at RT: (tumor sections) perforin – 1:100 for 30 min, SOX10 – 1:100 for 60 min, CD161 – 1:4000 for 5 min, cPARP-1 – 1:100 for 15 min, CD4 – 1:500 for 15 min, CD8α –1:250 for 15 min; (TMA sections) F4/80 – 1:50 for 45 min, CD69 – 1:50 for 30 min, CD19 – 1:500 for 15 min, CD3 – 1:500 for 15 min, CD4 – 1:500 for 15 min, CD8α – 1:250 for 15 min. Following 1X tris-buffered saline washes, ~200 µL diluted rat or rabbit secondary antibody (Abcam) was applied to each slide and incubated for 10 min. Following a 1X tris-buffered saline wash, Opal dyes were applied at 1:100 dilution for 10 min in 1X Amplification Diluent (Akoya Biosciences): (tumor sections) perforin – Opal dye 520, SOX10 – Opal dye 540, CD161 – Opal dye 570, cPARP-1 – Opal dye 620, CD4 – Opal-dye 650, CD8α – Opal dye 690; (TMA sections) F4/80 – Opal dye 520, CD69 – Opal dye 540, CD19 – Opal dye 570, CD3 – Opal dye 620, CD4 – Opal dye 650, CD8α – Opal dye 690 (all from Akoya Biosciences). Finally, stained sections were incubated in diluted DAPI (Akoya Biosciences) for 10 min at RT for nuclear labeling and mounted on glass coverslips with Prolong Gold Antifade Reagent (Invitrogen) for imaging. Imaging was performed on whole tumor slides at 4× and then regions of interest (ROIs) were selected and imaged at 20× using a Vectra multispectral imaging system (Akoya Biosciences) – 8 ROIs per tumor, 5 at tumor exterior and 3 at tumor interior. Imaging was performed on the TMA by taking a 3×3 grid within each spleen or lymph node core, at 20× using a Vectra multispectral imaging system (Akoya Biosciences). A spectral library was also generated to separate spectral curves for each of the fluorophores. One experimental replicate was performed.

Multiplex immunofluorescence data analysis

Resulting multispectral images were analyzed using Nuance and inForm software (Akoya Biosciences). A spectral library algorithm was created using multispectral image cubes from Vectra to define distinctive spectral curves for each fluorophore, chromogen, and counterstain to adjust for background effects and accurately quantify positive staining of biomarkers using inForm software. InForm software analysis allows objective counting of cell populations and biomarkers and increases the accuracy of the statistical analysis. Algorithms for subcellular compartment separation were created by machine learning to identify nuclei and membrane, respectively, to accurately assign associations for positive staining to a specific compartment in the tumor microenvironment. To create each algorithm, 10% of the total image dataset was used for each experiment. Positivity thresholds were set for each antibody in each tissue type (tumor, spleen, lymph node).

QUANTIFICATION AND STATISTICAL ANALYSIS

All details on statistical tests, replicates, etc. can be found within the figure captions.

Mice survival probabilities were estimated using the Kaplan-Meier method. Pairwise log-rank tests with Benjamini-Hochberg adjustment were used to compare survival curves of the different treatment groups within each experiment. Tumor volumes were considered "missing" after mouse death. All remaining available data was used for the tumor growth analysis. Linear mixed models accounting for mouse id as a random intercept were fit for each experiment, with treatment, time in days, and the interaction of treatment & day included as fixed effects. The outcome, tumor volume, was transformed by $\log_{10}(y+0.0001)$ to satisfy model assumptions. The small constant (0.0001) was added to handle tumor volumes of 0. The tumor growth rates of the treatment groups within each experiment were compared using pairwise contrasts and adjusted for multiple comparisons using Tukey's method. Differences in primary and rechallenge cures were calculated via Fisher exact test. Mouse analyses were carried out in R v4.1.2.

Flow cytometry results are represented as scatter dot plots showing mean (bar) ± standard deviation. Each dot represents a single mouse tumor. A one-way ANOVA was calculated with Šídák's multiple comparisons test, $\alpha = 0.05$ (GraphPad Prism v10.4).

In vivo metabolic imaging results are represented as dot plots showing mean ± standard deviation, stratified by treatment group and imaging day. Each dot represents a single tumor or CD8 T cell. A multi-level linear mixed effects model with animal specific random effects was used to evaluate differences in metabolism parameters on single-cell levels between treatment groups and imaging day assessment time points. Treatment group, day, and the interaction effect between day and treatment groups were included as predictor variables. A compound symmetry correlation structure was used to account for correlations between subsamples within each animal. Model assumptions were verified by examining residual plots. All reported p-values are two-sided and $p<0.05$ was used to define statistical significance. Statistical analyses were conducted using SAS software v9.4 (SAS Institute, Cary NC). Effect size was also calculated to assess differences in optical metabolic imaging parameters between treatment groups using Glass's Δ because comparisons of very large sample sizes of individual cells nearly always pass traditional significance tests unless the population effect size is truly zero. Glass's Δ is defined as: (mean experimental group – mean control group)⁄standard deviation control group. A Glass's Δ > 0.8 was chosen to indicate significant effect size based on previous studies.[66,122,123]

In vitro metabolic imaging results are represented as dot plots showing mean ± standard deviation. Each dot represents a single tumor cell. Mann–Whitney statistical tests for non-parametric, unpaired comparisons were performed to assess differences in metabolic parameters between treatment groups (GraphPad Prism v10.4). Effect size was also calculated.

Single-cell RNA sequencing results are represented as UMAPs, heatmaps (relative gene expression), Dot Plots (average gene expression), and violin plots showing mean ± standard deviation. Differences between specific metabolic genes across cell clusters were calculated via Wilcoxon rank-sum test with Benjamini-Hochberg correction (R v4.4.2).

Multiplex immunofluorescence results are represented as scatter dot plots showing mean (bar) ± standard deviation, where each dot represents a single field of view (FOV). Data is also represented as line plots showing the average value across several FOV. A one-way ANOVA was calculated with Šídák's multiple comparisons test, $\alpha = 0.05$ (GraphPad Prism v10.4).